Study of Low Energy Ytterbium Atom-Ion Charge Transfer Collisions Using a Surface-Electrode Trap

by

Thaned Pruttivarasin

Submitted to the Department of Physics
in partial fulfillment of the requirements for the degree of

Bachelor of Science in Physics

at the

MASSACHUSETTS INSTITUTE OF TECHNOLOGY

June 2008

Author . . . .
Department of Physics
May 9, 2008

Certified by . . . .
Prof. Vladan Vuletić
Lester Wolfe Associate Professor of Physics
Thesis Supervisor, Department of Physics

Accepted by . . . .
Prof. David E. Pritchard
Senior Thesis Coordinator, Department of Physics

Study of Low Energy Ytterbium Atom-Ion Charge Transfer Collisions Using a Surface-Electrode Trap

by

Thaned Pruttivarasin

Submitted to the Department of Physics
on May 9, 2008, in partial fulfillment of the
requirements for the degree of
Bachelor of Science in Physics

Abstract

We demonstrate a new isotope-selective system to measure low energy charge transfer collisions between ytterbium ions and atoms in the range of collisional energy from 2.2×10^{-5} eV to 4.3×10^{-3} eV, corresponding to effective temperature from 250 mK to 50 K. The charge transfer collisions are observed by spatially overlapping the $^{172}\mathrm{Yb}^{+}$ ions in the surface-electrode trap and $^{174}\mathrm{Yb}$ atoms in the magneto-optical trap, and measuring ion loss. We confirm that, in the Langevin regime, the charge transfer collisional rate is independent of the collisional energy. The measured Langevin cross section is consistent with a theoretical value for the ytterbium atomic polarizability of 143 a.u., as calculated by Zhang and Dalgarno [1].

Thesis Supervisor: Prof. Vladan Vuletić
Title: Lester Wolfe Associate Professor of Physics

Acknowledgments

This thesis is only a part of what I have learnt from working in Vuletić group at MIT. It is a priceless experience for me to be a part of a group of brilliant scientists in the corridor of the second floor of building 26. I would like to thank especially Prof. Vladan Vuletić and people in the ion trapping experiment. Vladan was generous enough to let me work in his lab since the last term of my freshmen year. I was in the 8.04 class taught by him and was stunned by his ability to convey and express his thoughts in the class. Working with him in the lab is even more rewarding. Many times, when there is a discussion in the group, Vladan took time to explain to me in the 8.04 language so that I could understand and follow. Marko Cetina and Andrew Grier are the two people that I interact with most during the time in the laboratory. I caused some stressful moments in the lab work but they always took time to really sit down and walk through the problem with me very professionally. I really cannot expect more from them and cannot describe in words how much I have learnt from them. Jon Campbell was in the lab during the first half of my career. His sense of humor really got me every time I spoke to him. Without him, the lab experience would not be as nice. Fedja Orucevic, who recently joined the group, also taught me a lot and, together with everyone mentioned above, helped me tremendously with the draft of the thesis. Jon Simon, Haruka Tanji, Saikat Ghosh, Monica Schleier-Smith and Ian Leroux are the people around the lab that I can count on every time I have any problem. Huanqian Loh, Brendan Shields, Yiwen Chu and David Brown are the fellow undergraduate “senpai” in the lab that kept me alive every time I talk to them. I also would like to thank everyone on the floor besides the people I mentioned above for a unique atmosphere of the MIT CUA.

I am indebted to all of my teachers. I would like to thank especially Prof. Lowell Lindgren, Prof. Mike Cuthbert and Prof. Peter Child of the Music Department for everything they taught me and for giving me free concert tickets to keep my mind well-adjusted. I would like to thank my physics teachers back in Thailand, especially A. Piyapong, A. Suwan and A. Wuthiphan for their kindness and mentorship. I would like to thank all the teachers at St. Gabriel College for a solid background in high school education.

I would like to thank everyone at MIT that I know or knows me for giving me a wonderful experience during these long but brief four years. I am grateful to all the Thai people that I know in USA, especially my fellow Thai Scholars. Thank you for an unforgettable memory.

Lastly, I would like to thank the members of my family for everything they have done for me. I love you all and I hope I did not let you down.

Contents

List of Figures

List of Tables

Chapter 1

Introduction

In modern cold atom experiments, one of the most widely used cooling techniques besides laser cooling is the so-called sympathetic cooling wherein particles of one type cool particles of another type by elastic collisions between the two species. This approach has been used to realize Bose-Einstein condensation using a buffer gas [5, 6]. Sympathetic cooling could also be very important for quantum computation experiments with cold ions. Here, it is important not to disturb the internal state of the ions which we prepare for the quantum gate operations. One way to achieve this is to have additional "refrigerator" ions or atoms which can be directly laser cooled, and then use them to sympathetically cool the main ions in the trap. The sympathetic cooling of ions with atoms is made difficult because of the possibility of inelastic collisions such as charge transfer. Understanding these limitations is an important step towards better performance of quantum computing experiments with ions. The goal of this experiment is to provide a step towards better understanding of atom-ion collisions, especially at low collisional energy relevant to cold atom and ion experiments since this range of collisional energies has not been achieved in any previous setup.

Our approach to studying collisions between atoms and ions at low energy is to confine ytterbium ions and atoms independently and let them interact with each other. We confine laser-cooled ions using a radio frequency (rf) electric field in a three-rod linear surface-electrode Paul trap. The atoms are confined in a magneto-optical trap (MOT). This allows us to attain collisional energies from 4.3×10^{-3} eV down to 2.2×10^{-5} eV.

The open geometry of the surface-electrode Paul trap allows us to easily adjust the overlap between the ions and atoms, controlling the atomic density seen by the ions.

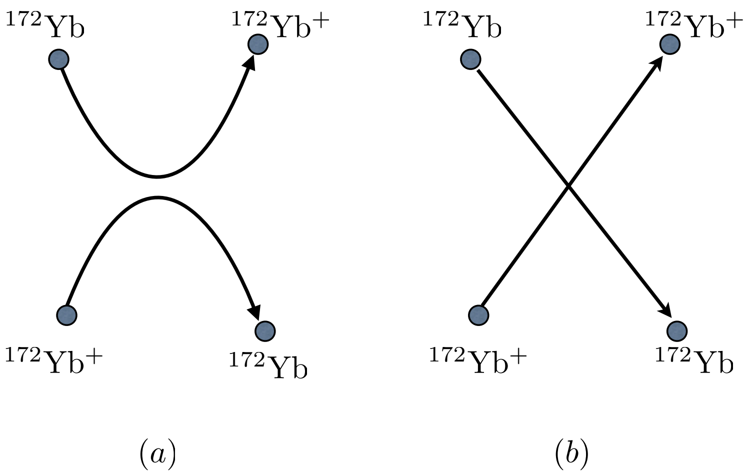

Figure 1-1: Collisions between ^{172}Yb and ^{172}Yb^{+} with two possible processes: (a) charge transfer happen; (b) elastic collisions (no charge transfer). Looking at the outcome, we cannot distinguish (a) from (b).

The position of the MOT is controlled by producing an off-set static magnetic field in the region around the MOT using a set of biased coils. The position of the ions, on the other hand, is controlled by applying electric potentials to the small electrodes around the ion trap. Since we control the positions of the ions and atoms through different mechanism, their positions can be varied independently of one another.

Our experimental setup also lets us have atoms in the MOT and ions in the trap of different species. This isotope selectivity is crucial since, as shown in Figure 1-1 and 1-2, charge transfer collisions can be distinguished from elastic (no charge transfer) collisions only in the case where atoms and ions are of different species. This robust isotope selectivity lets us study the atom-ion collisions of any combinations of ytterbium isotopes. The detecting system is designed in such a way that the fluorescence signal from the ions is lost whenever charge transfer collisions happen. With this we can measure the ion-atom charge exchange rate at a number of different effective atom densities.

The ion loss rate directly depends on the charge transfer cross section. At sufficiently low collisional energy, the ion loss rate due to charge transfer collisions is predicted to be independent of the collisional energy, and directly related to the atomic polarizability of ytterbium. The goal of our experiment is to confirm that the

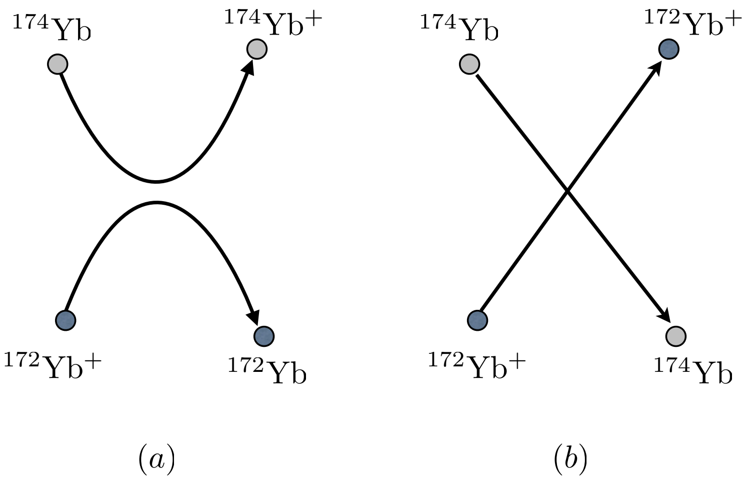

Figure 1-2: Collisions between ^{174}Yb and ^{172}Yb$^+$ with two possible processes: (a) charge transfer happen; (b) elastic collisions (no charge transfer). In this case, we can distinguish (a) from (b) by looking at the outcome.

charge transfer collisional rate is indeed independent of the collisional energy. This also provides a direct way to measure the ytterbium atomic polarizability which will be compared to the theoretical value calculated by Zhang and Dalgarno [1].

In this thesis, we start in Chapter 2 by developing both the classical and the quantum theory of charge transfer collisions. The results of the two approaches will be compared; and the ion loss rate due to charge exchange is derived at the end of this chapter. In Chapter 3, the theory of laser cooling and trapping of neutral atoms are presented. Chapter 4 follows Chapter 3 by presenting the trapping mechanism for ions and our surface-electrode trap geometry. The micromotion energy of the ions, which is important in adjusting the collisional energy of the ions, is discussed at the end of this chapter. All components in our experiment are put together in Chapter 5. Chapter 6 shows the measurements and data analysis of the atomic polarizability of ytterbium. The result will be presented at the end of this chapter. Finally, Chapter 7 summarizes the experiment and discusses some of the possible future work.

Chapter 2

Atom-Ion Collision Theory

Atom-ion collisions can generally be divided into two categories. The first one is normal elastic collisions where there is no change in internal structures of the colliding particles. Normally we denote this type of reaction by

$$A + B \rightarrow A + B. \tag{2.1}$$

In reality, this is not the only possible outcome of the collisions. We cannot ignore the interaction between the two colliding particles besides mutual long-range interaction. For example, an electron from particle A might hop to particle B provided that A and B are close enough to each other. This change in internal structure after collisions is generally referred to as inelastic collisions, which is the second category of atom-ion collisions. In our discussion we are particularly interested in the case where there is a possibility that an electron from an atom hops to an ion. This is denoted by

$$A^+ + B \rightarrow A + B^+ \tag{2.2}$$

for different ions and atoms, or

$$A^+ + A \rightarrow A + A^+ \tag{2.3}$$

for ions in their parent gases.

Charge transfer can happen through either inner-core collisions or tunneling of an electron. The first process is well-described by the classical theory of scattering. The second process can be described only by resorting to quantum mechanics. The goal of this chapter is to discuss and obtain the expression of the cross section for charge transfer collisions. We begin by presenting the classical theory of scattering and derive the Langevin cross section. The quantum mechanical treatment is then discussed by first looking at the electronic structure of a simple molecule. Then the partial wave analysis is briefly summarized by before we derive the charge transfer cross section for both inner-core collisions and tunneling, which are the case for low and high collisional energy, respectively. We will see that both classical and quantum mechanical treatments give the same result for the inner-core collisions. Finally we derive the ion loss rate under charge transfer collisions.

2.1 Classical Theory for Polarization Field: Langevin Cross Section

We first look at the problem using classical mechanics and electromagnetic theory. Polarization potential which describes the interaction between atoms and ions will be derived first. Then we will see how such potential influences the trajectories of the particles in the scattering problem.

2.1.1 Atom-Ion Polarization Potential

Although a neutral atom has no charge, as its name implies, an atom in electric field will have an induced dipole moment (or higher induced multipole moments). Normally, we can write

$$\vec{p} = \alpha \vec{E} \tag{2.4}$$

where $\vec{p}$ is the induced dipole moment, α is the atomic polarizability, and $\vec{E}$ is the electric field. Generally α is a tensor quantity. In our case, we can write it in the form of vector because the ground state of ytterbium atom or ion has a spherical symmetry.

Consider a system of one atom and one ion both with mass m. In our system, we can restrict ourselves to a singly ionized ion; so its charge is simply $+e$. Let $\vec{r}_a$ and $\vec{r}_i$ be position vectors of the atom and ion, respectively, as in Figure 2-1. The electric field produced by the ion at the atom is given by

$$\vec{E}(\vec{r}_a, \vec{r}_i) = \frac{e}{4\pi\epsilon_o} \frac{\vec{r}_a - \vec{r}_i}{|\vec{r}_a - \vec{r}_i|^3} \tag{2.5}$$

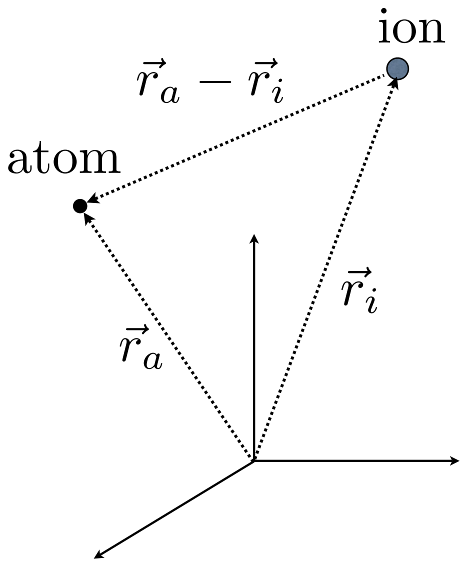

Figure 2-1: System of a pair of atom and ion.

where ϵ_o is the permittivity in vacuum. The induced dipole moment of the atom is now given by

$$\vec{p}(\vec{r}_a, \vec{r}_i) = \alpha \vec{E}(\vec{r}_a, \vec{r}_i) = \frac{e\alpha}{4\pi\epsilon_o} \frac{\vec{r}_a - \vec{r}_i}{|\vec{r}_a - \vec{r}_i|^3}. \tag{2.6}$$

We assume that the electric field of the ion seen by the atom is uniform throughout the volume of the atom.[1] The electric field due to an induced atomic dipole can be written as

$$\vec{E}_{\text{dip}}(\vec{r}) = \frac{1}{4\pi\epsilon_o} \frac{1}{r^3} (3(\vec{p} \cdot \hat{r})\hat{r} - \vec{p}) \tag{2.7}$$

where $\vec{r}$ is the position vector pointing from the position of the atom. In order to see the mutual potential between the ion and atom, we set $\vec{r}_a = 0$ and let $\vec{r} = \vec{r}_i$. This is to put the atom at the origin and consider only the distance between the two, which now depends only on $\vec{r}_i$. With these conditions, (2.6) and (2.7), we can write the electric field of the dipole seen by the ion as

---

[1] This is generally called the dipole approximation.

$$
\begin{aligned}
\vec{E}_{\text{dip-ion}}(\vec{r_i}) &= \frac{1}{4\pi\epsilon_o}\frac{1}{|\vec{r_i}|^3}(3(\vec{p}(\vec{r_i})\cdot\hat{r}_i)\hat{r}_i - \vec{p}(\vec{r_i})) \\
&= -\frac{e\alpha}{(4\pi\epsilon_o)^2}\frac{1}{|\vec{r_i}|^3}(3(\frac{\vec{r_i}}{|\vec{r_i}|^3}\cdot\hat{r}_i)\hat{r}_i - \frac{\vec{r_i}}{|\vec{r_i}|^3}) \\
&= -\frac{e\alpha}{(4\pi\epsilon_o)^2}\frac{2}{|\vec{r_i}|^5}\hat{r}_i. \qquad (2.8)
\end{aligned}
$$

Then the force on the ion is simply

$$\vec{F}_{\text{dip-ion}}(\vec{r_i}) = -\frac{e^2\alpha}{(4\pi\epsilon_o)^2}\frac{2}{|\vec{r_i}|^5}\hat{r}_i. \qquad (2.9)$$

Notice that the sign of the force is negative. This indicates that the force between the atom and ion is attractive. The potential energy can be calculate according to the definition

$$
\begin{aligned}
U_{\text{dip-ion}}(r) &= \int_r^\infty \vec{F}_{\text{dip-ion}}(\vec{r_i})\cdot d\vec{r_i} \\
&= \int_r^\infty -\frac{e^2\alpha}{(4\pi\epsilon_o)^2}\frac{2}{|\vec{r_i}|^5}\hat{r}_i\cdot d\vec{r_i} \\
&= -\frac{2e^2\alpha}{(4\pi\epsilon_o)^2}\int_r^\infty \frac{1}{|\vec{r_i}|^5}dr_i \\
&= -\frac{e^2\alpha}{32\pi^2\epsilon_o^2}\frac{1}{r^4}. \qquad (2.10)
\end{aligned}
$$

The polarization potential between the atom and ion is described by an inverse-fourth-power interaction. Following the guideline in the appendix, this potential can be written in atomic units as

$$U_{\text{dip-ion}}(r) = -\frac{e^2\alpha}{2r^4}. \qquad (2.11)$$

For most atoms, and especially for ytterbium, α is positive. This provides an attractive potential between ions and atoms.

2.1.2 Classical Atom-Ion Scattering Problem

Any classical scattering problem with central force can be analyzed easily using the standard treatment in any classical mechanics textbook [7]. For reference, we will repeat the main results without going into many details.

Distance of Closest Approach

In any two-body collisions, we can reduce the problem to one body in the center of mass frame and use instead the reduced mass, μ, defined as

$$\frac{1}{\mu} = \frac{1}{m_1} + \frac{1}{m_2}, \tag{2.12}$$

where m_1 and m_2 are the masses in the system. In this reduced problem, the position coordinate, r, is the separation between the two particles. Let us consider the situation in Figure 2-2-a. Let us place the atom at the origin and consider an ion approaching from a large distance. The impact parameter is given by b, and the relative velocity of the ion at infinity is given by v_i. If b is not too small, the ion will follow a trajectory similar to that in Figure 2-2-a. The distance of closest approach, r_c, is the distance between the ion and the origin at the point where the velocity vector and the position vector of the ion from the atom are perpendicular. Using the conversation of mechanical energy, we arrive at the first condition:

$$\frac{1}{2}\mu v_i^2 = \frac{1}{2}\mu v_c^2 - \frac{k\alpha}{r_c^4}, \tag{2.13}$$

where μ, again, is the reduced mass, v_c is the relative velocity at the point of closest approach, and $k = e^2/32\pi^2\epsilon_o^2$. Since the potential in our problem is central, we arrive at the second condition using the conservation of angular momentum around the point of the atom:

$$\mu v_i b = \mu v_c r_c. \tag{2.14}$$

Under these two conditions, by eliminating v_c, we get

$$r_c^4 - b^2 r_c^2 + \frac{2k\alpha}{v_i^2\mu} = 0. \tag{2.15}$$

Then,

$$r_c^2 = \frac{b^2 \pm \sqrt{b^4 - 8k\alpha/v_i^2\mu}}{2}. \tag{2.16}$$

Let us now assume that the term under the square root is positive. We will come back to the case where it is negative later. Now we can take square root of the whole expression again. Using the condition that r_c cannot be negative, we arrive at

$$r_c = \frac{b}{\sqrt{2}} \left[1 \pm \sqrt{1 - \frac{8k\alpha}{b^4 v_i^2 \mu}} \right]^{1/2} . \tag{2.17}$$

What is left to be decided is the "±" sign in front of the square root. Suppose the atom has negative polarizability, i.e., $\alpha < 0$, then the square root term is larger than one. Since r_c has to be real, then we can simply choose "+" in front of the square root. However, this is not necessary for $\alpha > 0$ because both signs give a real value of r_c. But suppose you have an ability to "tune" the polarizability gradually and continuously from negative value to zero and eventually to positive value (going from Figure 2-2-c to 2-2-b and then 2-2-a). In this case you are also tuning the value of r_c. Our physical reasoning says that there is no reason for a discontinuity when going from negative α to positive α. Mathematically, $dr_c/d\alpha$ must be finite at $\alpha = 0$. Hence, we can safely say that for any value of α, the closest distance between the ion and atom is given by [2]

$$r_c = \frac{b}{\sqrt{2}} \left[1 + \sqrt{1 - \frac{8k\alpha}{b^4 v_i^2 \mu}} \right]^{1/2} . \tag{2.18}$$

Charge Transfer Process

If the ion is close enough to the atom, a valence electron of the atom will have a probability of jumping to the ion. This charge transfer process can happen if the distance between the atom and ion is closer than the threshold distance, r_t. From (2.18), we can immediately see that r_c cannot be smaller than $b/\sqrt{2}$ for any given v_i. If r_t is larger than $b/\sqrt{2}$, charge transfer can happen. What if r_t is less than $b/\sqrt{2}$? Let us look at (2.18) more closely. We have assumed that the term under the square root is positive. What does it mean if it is negative, i.e.,

$$\frac{8k\alpha}{b^4 v_i^2 \mu} > 1, \tag{2.19}$$

which is the condition when r_c has no real root? In this case, there is no closest distance between the atom and ion and there is no point along the trajectory that

---

[2] We can also obtain the expression for the distance of closest approach by looking at the effective potential and calculate the turning point of the projectile in that potential.

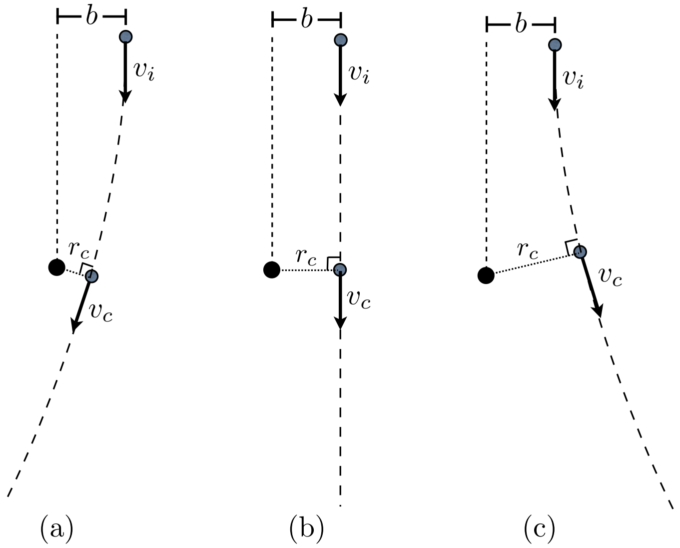

Figure 2-2: Atom-ion scattering with (a) positive atomic polarization (attractive potential), (b) zero polarizability and (c) negative polarizability (repulsive potential) at a fixed value of impact parameter, b. As we tune the value of α from negative to positive (from (c) to (a)), the distance of closest approach, r_c, must be continuous.

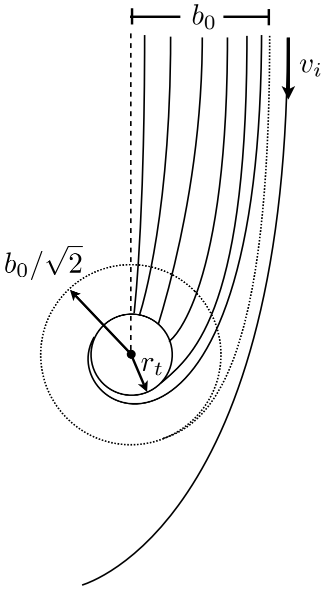

Figure 2-3: Selected trajectories of various impact parameters. The critical impact parameter, b_0, is given as a function of v_i.

gives $\vec{v} \cdot \vec{r} = 0$. If the atom has no internal structure, and our particles have no size, then the ion will spiral into the atom with the limit of the trajectory approaching the origin.[3] However, atomic internal structure will eventually push the ion outwards, and prevent the head-on collisions between the ion and atom.

If r_t, the threshold distance for charge transfer process, is less than $b/\sqrt{2}$, then the only way that the ion can get to this threshold distance is to follow the spiral path. Namely, for any given v_i, the impact parameter of the ion must be less than a critical value, b_0, where, from (2.19),

$$b_0^4 = \frac{8k\alpha}{v_i^2 \mu}. \tag{2.20}$$

Charge Transfer Cross Section

In the collisions at low temperature, v_i is always low enough such that $b_0/\sqrt{2}$ is a lot greater than r_t. As in Figure 2-3, as long as the impact parameter is less than b_0, it is guaranteed that the ion will reach the threshold distance r_t. The cross section

---

[3] Note that conservation of angular moment prevents the ion from passing the origin. The limit of the trajectory, however, is exactly the origin where the atom resides.

area where spiral orbits are guaranteed to happen is called the Langevin cross section. This was first derived by Langevin in 1905 [8]. It is simply given by

$$\sigma_{\text{Langevin}} = \pi b_0^2. \tag{2.21}$$

For the ion within the threshold value r_t, let us denote by p_c the probability that charge transfer happens. We can then take the charge transfer cross section to be

$$\sigma_{\text{ch}} = p_c \pi b_0^2 = p_c \pi \sqrt{\frac{8k\alpha}{v_i^2 \mu}}. \tag{2.22}$$

We can also write the charge transfer cross section in terms of collisional energy, $E_c = \frac{1}{2}\mu v_i^2$, as

$$\sigma_{\text{ch}} = p_c \pi \sqrt{\frac{4k\alpha}{E_c}}. \tag{2.23}$$

If the collisional energy is high, then r_t will be greater than $b_0/\sqrt{2}$ and we cannot simply take the charge transfer cross section to be the Langevin cross section. In this case, the charge transfer cross section is given instead by

$$\sigma_{\text{ch}} = (a \ln E_c - b)^2, \tag{2.24}$$

where a and b are constants [9, 10, 11]. Since the derivation of this expression requires quantum mechanical formulation, we will discuss this after we present all the relevant tools in the following sections.

2.2 Molecular Electronic Configuration

To start our discussion of the atom-ion collisions in the quantum mechanical formulation, we first look at the molecular electronic configuration of an atom-ion molecule. In the simplest case, we have a proton colliding with a hydrogen atom. There are three particles in the system: one electron and two protons. The usual hydrogenic wave function might not be adequate to describe the system, since there is an extra proton in the problem. In this simplest collisional configuration, it is helpful to understand the nature of molecular structure of a hydrogen molecular ion, H_2^+. The problem of ytterbium atom-ion collisions can be thought of in the same way, since the three particles in the system are one electron and two singly ionized ytterbium

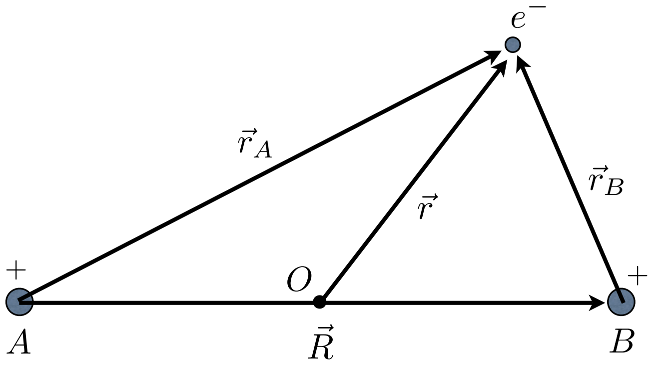

Figure 2-4: Coordinate system for the hydrogen molecular ion.

ions.

2.2.1 The Hydrogen Molecular Ion

Although the two protons in H_2^+ are indistinguishable, we assume that we can tell them apart by assigning labels onto them. Let the two protons be denoted by A and B. In the center-of-mass frame, the origin is taken to be the mid-point between the two protons. This frame is, to a very good approximation, an inertial frame since the mass of an electron is excessively small compared to that of a proton. We denote $\vec{R}$ to be the vector pointing from A to B, $\vec{r}$ to be the position of the electron relative to the origin, and $\vec{r}_A$ and $\vec{r}_B$ to be the relative positions of the electron with respect to A and B, respectively. This is illustrated in Figure 2-4.

The time-independent Schrödinger equation of this system is given by

$$\left[-\frac{\hbar^2}{2m_e}\nabla_r^2 - \frac{e^2}{4\pi\epsilon_0}\frac{1}{r_A} - \frac{e^2}{4\pi\epsilon_0}\frac{1}{r_B} + \frac{e^2}{4\pi\epsilon_0}\frac{1}{R}\right]\Phi = E\Phi. \tag{2.25}$$

Now it is convenient from now on to work in atomic units (see Appendix C). We now rewrite the Schrödinger equation to be

$$\left[-\frac{1}{2}\nabla_r^2 - \frac{1}{r_A} - \frac{1}{r_B} + \frac{1}{R}\right]\Phi = E\Phi. \tag{2.26}$$

Let us look closely to the wave function Φ. This wave function actually depends on $\vec{R}$ and $\vec{r}$. Those two are the only variables in the system, and $\vec{r}_A$ and $\vec{r}_B$ can be written in terms of $\vec{R}$ and $\vec{r}$. We can interchangeably write either $\Phi(\vec{R},\vec{r})$ or $\Phi(\vec{r}_A,\vec{r}_B)$ for the wave function of the electron.

According to Bransden and Joachain [12], we can now propose that if $R=|\vec{R}|$ is large, i.e., the two protons are very far apart, then the electron will be either attached to proton A or proton B. If the electron is attached proton A, at large R,

$$\Phi(\vec{R},\vec{r}) = \psi_{1s}(r_A), \tag{2.27}$$

where $r_A=|\vec{r}_A|$, and

$$\psi_{1s}(r') = \frac{1}{\sqrt{\pi}}e^{-r'} \tag{2.28}$$

is the ground state wave function of hydrogen and r' is the distance between the electron and the nucleus. Looking at Figure 2-4, we notice that the total wave function, $\Phi(\vec{R},\vec{r})$ must have a symmetry when setting $\vec{r}$ to $-\vec{r}$.[4] The wave function $\psi_{1s}(r_A)$ alone does not have that symmetry. We can, however, construct trial wave functions from linear combinations of $\psi_{1s}(r_A)$ and $\psi_{1s}(r_B)$. The wave function that is left unchanged under reflection is called "gerade" state, which is given by

$$\Phi_g(\vec{R},\vec{r}) = \frac{1}{\sqrt{2}}(\psi_{1s}(r_A)+\psi_{1s}(r_B)). \tag{2.29}$$

The wave that changes the sign under reflection is called "ungerade" state, which is given by

$$\Phi_u(\vec{R},\vec{r}) = \frac{1}{\sqrt{2}}(\psi_{1s}(r_A)-\psi_{1s}(r_B)). \tag{2.30}$$

Note that these trial wave functions are likely to be true only at large R. However, we can use them and try to solve for eigenenergies. We now have to evaluate

$$E_{g,u}(R) = \frac{\int \Phi^*_{g,u}(\vec{R},\vec{r})H\Phi_{g,u}(\vec{R},\vec{r})d\vec{r}}{\int |\Phi_{g,u}(\vec{R},\vec{r})|^2 d\vec{r}}. \tag{2.31}$$

Evaluation of the integrals involved is given in Appendix D. The results are

$$E_g(R) = E_{1s} + \frac{1}{R}\frac{(1+R)e^{-2R}+(1-\frac{2}{3}R^2)e^{-R}}{1+(1+R+\frac{1}{3}R^2)e^{-R}}, \tag{2.32}$$

---

[4] In our case where the proton A and B are identical, this is equivalent to flipping the two nuclei.

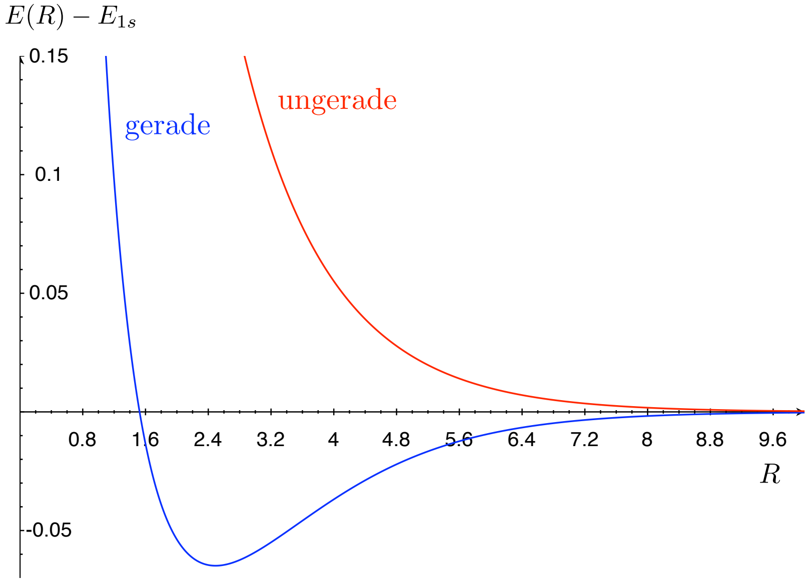

Figure 2-5: Plot of effective potential of gerade and ungerade states of hydrogen molecular ion. Energy and distance are measured in atomic units.

and

$$E_u(R) = E_{1s} + \frac{1}{R}\frac{(1+R)e^{-2R} - (1-\frac{2}{3}R^2)e^{-R}}{1-(1+R+\frac{1}{3}R^2)e^{-R}} \tag{2.33}$$

where E_{1s} is the ground state energy of hydrogen, -13.6 eV or -0.5 a.u. Figure 2-5 shows the visualization of the energy of the two states with varying distance, R. Although our calculation is not exact, the exact solution does not depart significantly from our model of potential curves [12]. We can see quite the distinct characteristic between gerade and ungerade states. For our case, the ungerade state does not have any bound state, so the molecule cannot be in this state. Bound states only occur in the gerade configuration. This energy curve is generally called an effective potential curve, meaning that it is the potential energy seen by one proton in the function of separation, R.

From our analysis of hydrogen molecular ion, we would like to motivate ourselves that the effective potential curve can be written in the asymptotic form at large R,

$$V_{g,u}(R) = V_{\text{disp.}}(R) \pm V_{\text{exc.}}(R), \tag{2.34}$$

where "disp." means "dispersion" and "exc." means "exchange" potential. The notions of “gerade” and “ungerade” wave functions are generally a good description for any molecular orbitals. This form of effective potential curve can also be generalized to other atom-ion collisions. Our case of the collisions between Yb^+ and Yb then can be discussed in the same way as in the hydrogen molecular ion.

2.2.2 Symmetry in Molecular Orbitals

In specifying the electronic structure of general two-nucleus molecules, we use the notation similar to what we are used to in atomic physics, namely, ${}^{2S+1}L_J$. Let us define the z-axis to be the line AB joining the two nuclei in Figure 2-4 and ignore electron spins for a moment. If L is the total orbital angular momentum of the electrons, the result from acting the operator L_z on the wave function Φ is

$$\begin{aligned} L_z\Phi &= M_L\Phi, \\ &= \pm\Lambda\Phi. \end{aligned} \tag{2.35}$$

where $M_L = 0, \pm1, \pm2...$ and $\Lambda = |M_L| = 0, 1, 2...$[5] This number Λ is important when we discuss the azimuthal dependence of the wave function. It appears in the form of $e^{\pm i\Lambda\phi}$ in the wave function analogous to m, the magnetic quantum number, in hydrogen wave function. We then assign letters to each value of Λ, namely,

$$\begin{aligned} \Lambda = 0 &\rightarrow \Sigma \\ \Lambda = 1 &\rightarrow \Pi \\ \Lambda = 2 &\rightarrow \Delta \\ \Lambda = 3 &\rightarrow \Phi. \end{aligned}$$

The Hamiltonian of the system is invariant under reflections in all planes containing AB or the z-axis. Suppose we have an operator A_y which changes y to $-y$ in the wave function and recall that $L_z = -i(x\partial y - y\partial x)$, we have

$$A_yL_z = -L_zA_y. \tag{2.36}$$

This means that for $\Lambda \neq 0$, the eigenvalue Λ will be changed to $-\Lambda$. These states where $\Lambda \neq 0$ are doubly degenerate since they are the solutions of the same energy [12].

---

[5] Note that we have worked in atomic units and $\hbar$ disappears.

For $\Lambda = 0$ states, simultaneous eigenstates of H, L_z and A_y can be constructed. Since the eigenvalues of A_y are ± 1, we then specify the state Σ to be Σ^+ for a state in which the wave function is left unchanged under reflection through the plane containing AB and Σ^- for the opposite case.

If the two nuclei are the same, then we have to impose a symmetry around point O in Figure 2-4. This is exactly what we did in the last section. If the wave function is left unchanged under flipping $\vec{r}$ to $-\vec{r}$ around this point, it is called "gerade" state and we write it as Σ_g. If it is the opposite case, i.e., flipping $\vec{r}$ to $-\vec{r}$ imposes a minus sign in front of the wave function, then it is called the "ungerade" state and we write it as Σ_u. In summary there are four Σ states for homonuclei diatomic molecule: Σ_g^+, Σ_g^-, Σ_u^+ and Σ_u^-. The following sections will pay close attention to the Σ_g^+ and Σ_u^+ states since they are the main contribution of the charge transfer collisions between ions and atoms.

2.3 Quantum Scattering Theory

Having obtained the potential curve between two nuclei, we can now turn to the problem of two-body scattering under any potential. We write a general potential to be $V(R)$, which depends only the distance R between the two nuclei.

2.3.1 The Asymptotic Stationary Wave Function

In the lab frame, if the position vectors of two nuclei with mass m_a and m_b are denoted by $\vec{r}_a$ and $\vec{r}_b$, respectively, the Hamiltonian in atomic units is given by

$$H = -\frac{1}{2m_a}\nabla^2_{r_a} - \frac{1}{2m_b}\nabla^2_{r_b} + V(\vec{r}_a - \vec{r}_b). \tag{2.37}$$

We can rewrite everything in the center-of-mass frame by using

$$\vec{r} = \vec{r}_a - \vec{r}_b, \tag{2.38}$$

$$\vec{R} = \frac{m_a\vec{r}_a + m_b\vec{r}_b}{m_a + m_b}, \tag{2.39}$$

$$M = m_a + m_b, \tag{2.40}$$

$$\mu = \frac{m_a m_b}{m_a + m_b}. \tag{2.41}$$

The Schrödinger equation now can be written as

$$\left(-\frac{1}{2M}\nabla_R^2 - \frac{1}{2\mu}\nabla_r^2 + V(r)\right)\Phi(\vec{r},\vec{R}) = E_t\Phi(\vec{r},\vec{R}), \tag{2.42}$$

where E_t is the total eigenenergy of the system. We now separate the two uncoupled coordinates by writing

$$\Phi(\vec{R},\vec{r}) = \phi(\vec{R})\psi(\vec{r}). \tag{2.43}$$

Now the full Schrödinger equation becomes

$$-\frac{1}{2M}\nabla_R^2\phi(\vec{R}) = E_{CM}\phi(\vec{R}), \tag{2.44}$$

$$\left(-\frac{1}{2\mu}\nabla_r^2 + V(r)\right)\psi(\vec{r}) = E\psi(\vec{r}), \tag{2.45}$$

$$E_t = E + E_{CM}. \tag{2.46}$$

We will carry on our analysis in the center-of-mass frame. We can see that the problem is reduced to the one-dimensional scattering problem for the relative separation r. Only now the mass is replaced by the reduced mass, μ. At long distance r, $V(r)$ should asymptotically tend to zero, and we have

$$E = \frac{k^2}{2\mu} \text{ (a.u.)}, \tag{2.47}$$

where k is the wave number defined in SI units to be $\vec{p}/\hbar$ where $\vec{p}$ is the linear momentum vector. We write the scaled potential to be

$$U(r) = 2\mu V(r). \tag{2.48}$$

Now the Schrödinger equation becomes

$$\left(\nabla_r^2 + k^2 - U(r)\right)\psi(\vec{r}) = 0. \tag{2.49}$$

We now propose that at large r, the wave function has the form

$$\psi(k,\vec{r}) \to A(k)\left(e^{i\vec{k}\cdot\vec{r}} + f(k,\theta,\phi)\frac{e^{ikr}}{r}\right) \tag{2.50}$$

where A is independent of r; and θ and ϕ are parameters in spherical coordinate defined by taking the z-axis along $\vec{k}$, the incident wave number. This is valid as long as $V(r)$ (or $U(r)$) goes to zero faster than r^{-1} [13].

2.3.2 Partial Wave Expansion

We now briefly summarize the partial wave expansion method. Let us now write Schrödinger equation in (2.49) using spherical coordinate. The Hamiltonian operator (not including the k^2 term) is given by

$$H = -\frac{1}{2\mu}\left(\frac{1}{r^2}\frac{\partial}{\partial r}\left(r^2\frac{\partial}{\partial r}\right) + \frac{1}{r^2\sin\theta}\frac{\partial}{\partial\theta}\left(\sin\theta\frac{\partial}{\partial\theta}\right) + \frac{1}{r^2\sin^2\theta}\frac{\partial^2}{\partial\phi^2}\right) + V(r). \quad (2.51)$$

The angular dependent part can be rewritten in terms of the angular momentum operator, L.[6] We can now write

$$H = -\frac{1}{2\mu}\left(\frac{1}{r^2}\frac{\partial}{\partial r}\left(r^2\frac{\partial}{\partial r}\right) - \frac{L^2}{r^2}\right) + V(r). \quad (2.52)$$

It is then natural to try to write the wave function in (2.49) to be the expansion of spherical harmonics, i.e.,

$$\psi(k,\vec{r}) = \sum_{l=0}^{\infty}\sum_{m=-l}^{+l} c_{lm}(k)R_{lm}(k,r)Y_{lm}(\theta,\phi), \quad (2.53)$$

where $R_{lm}(k,r)$ satisfies the radial equation

$$-\frac{1}{2\mu}\left(\frac{1}{r^2}\frac{\partial}{\partial r}\left(r^2\frac{\partial}{\partial r}\right) - \frac{l(l+1)}{r^2}\right)R_l(k,r) + V(r)R_l(k,r) = ER_l(k,r). \quad (2.54)$$

We drop the subscript m because there is no m dependence in the Hamiltonian. Following the standard approach, we write

$$u_l(k,r) = rR_l(k,r), \quad (2.55)$$

---

[6] See Appendix E for details on the angular momentum operator and the spherical harmonics.

and obtain (2.49) in the form

$$\left(\frac{d^2}{dr^2} + k^2 - \frac{l(l+1)}{r^2} - U(r)\right) u_l(k,r) = 0. \tag{2.56}$$

We now look at the region where r is very large such that we can ignore the potential term, $U(r)$. Our radial equation becomes

$$\left(\frac{d^2}{dr^2} + k^2 - \frac{l(l+1)}{r^2}\right) u_l(k,r) = 0. \tag{2.57}$$

The general solution is

$$u(k,r) \rightarrow kr[C_l^{(1)}(k) j_l(kr) + C_l^{(2)}(kn_l(kr)], \tag{2.58}$$

where $j_l(kr)$ and $n_l(kr)$ are the spherical Bessel and Neumann functions, respectively. Looking at the asymptotic form of the spherical Bessel and Neumann functions,

$$j_l(x) \rightarrow \frac{1}{x} \sin{(x - \frac{1}{2} l\pi)}, \tag{2.59}$$

$$n_l(x) \rightarrow -\frac{1}{x} \cos{(x - \frac{1}{2} l\pi)}, \tag{2.60}$$

we can write

$$u_l(k,r) \rightarrow A_l(k) \sin{(kr - \frac{1}{2} l\pi + \delta_l(k))}, \tag{2.61}$$

with

$$A_l(k) = \sqrt{[C_l^{(1)}(k)]^2 + [C_l^{(2)}(k)]^2} \tag{2.62}$$

and

$$\tan \delta_l(k) = -\frac{C_l^{(2)}(k)}{C_l^{(1)}(k)}. \tag{2.63}$$

Let us now return to our asymptotic wave function in the previous section. Again, we have, at large r,

$$\psi(k, \vec{r}) \rightarrow A(k) \left(e^{i\vec{k}\cdot\vec{r}} + f(k,\theta,\phi) \frac{e^{ikr}}{r} \right) \tag{2.64}$$

and we take the expansion of the exponential term by writing

$$e^{i\vec{k}\cdot\vec{r}} = e^{ikz} = \sum_{l=0}^{\infty}(2l+1)i^l j_l(kr)P_l(\cos\theta), \tag{2.65}$$

where $P_l(\cos\theta)$ is the Legendre polynomials. With the definition of the spherical harmonics given in Appendix E, we have

$$P_l(\cos\theta) = \sqrt{\frac{4\pi}{2l+1}}Y_{l,0}(\theta,\phi). \tag{2.66}$$

Now we substitute these expressions into (2.64), using the asymptotic form of the spherical Bessel functions, and obtain

$$\begin{aligned}\psi(k,\vec{r}) &\to A(k)\left(\sum_{l=0}^{\infty}(2l+1)i^l\frac{\sin(kr-l\pi/2)}{kr}P_l(\cos\theta) + f(k,\theta,\phi)\frac{e^{ikr}}{r}\right), \\ &\to A(k)\left(\sum_{l=0}^{\infty}(2l+1)i^l\frac{e^{i(kr-l\pi/2)}-e^{-i(kr-l\pi/2)}}{2ikr}\sqrt{\frac{4\pi}{2l+1}}Y_{l,0}(\theta,\phi)\right. \\ &\qquad\left.+f(k,\theta,\phi)\frac{e^{ikr}}{r}\right).\end{aligned} \tag{2.67}$$

We now want to compare this expression to

$$\psi(k,\vec{r}) = \sum_{l=0}^{\infty}\sum_{m=-l}^{+l}c_{lm}(k)R_{lm}(k,r)Y_{lm}(\theta,\phi).$$

By using the fact that $R_{lm}(k,r) = r^{-1}u_l(k,r)$ for large r and (2.61), we have

$$\psi(k,\vec{r}) = \sum_{l=0}^{\infty}\sum_{m=-l}^{+l}c_{lm}(k)A_l(k)\frac{e^{i(kr-l\pi/2+\delta_l)}-e^{-i(kr-l\pi/2+\delta_l)}}{2ir}Y_{lm}(\theta,\phi). \tag{2.68}$$

By comparing the coefficients of the incoming wave (the e^{-ikr} terms) of (2.67) and (2.68), we have

$$c_{lm}(k) = (2l+1)\frac{A(k)}{kA_l(k)}\sqrt{\frac{4\pi}{2l+1}}i^l e^{(i\delta_l)}\delta_{m,0}. \tag{2.69}$$

By matching the outgoing wave (the e^{ikr} terms) we arrive at

$$f(k,\theta) = \frac{1}{2ik}\sum_{l=0}^{\infty}(2l+1)(e^{2i\delta_l(k)}-1)P_l(\cos\theta). \tag{2.70}$$

The total wave function now can be written in the following form:

$$\begin{aligned}\psi(k,\vec{r}) &\to A(k)\left(e^{i\vec{k}\cdot\vec{r}} + f(k,\theta,\phi)\frac{e^{ikr}}{r}\right) \\ &\to A(k)\left(e^{i\vec{k}\cdot\vec{r}} + \frac{1}{2ik}\sum_{l=0}^{\infty}(2l+1)(e^{2i\delta_l(k)}-1)P_l(\cos\theta)\frac{e^{ikr}}{r}\right). \end{aligned} \tag{2.71}$$

This form will be useful in the next section when we try to calculate total cross section.

2.3.3 Scattering Cross Section

We now follow the argument by Griffith [14] to determine the scattering cross section. The quantity $f(k,\theta,\phi)$ is usually called the scattering amplitude for a reason. This amplitude tells us the probability of scattering in a given direction θ. Let us have a small area $d\sigma$ that the incident particles hit during the time dt and at velocity v, and the probability of that this event will happen is given by

$$dP = |\psi_{\text{incident}}|^2 dV = |A(k)|^2(vdt)d\sigma. \tag{2.72}$$

These particles will undergo scattering and later they will be emerging at the corresponding solid angle $d\Omega$ with the same probability–only now it can also be written as

$$dP = |\psi_{\text{scattered}}|^2 dV = \frac{|A(k)|^2|f(k,\theta,\phi)|^2}{r^2}(vdt)r^2 d\Omega. \tag{2.73}$$

It then, by equating the two probabilities, follows that

$$d\sigma = |f(k,\theta,\phi)|^2 d\Omega. \tag{2.74}$$

So the total cross section is given by

$$\sigma_t = \int |f(k,\theta,\phi)|^2 d\Omega. \tag{2.75}$$

We can use (2.70) and try to calculate the total cross section. The integral that we need to evaluate is

$$
\begin{aligned}
\sigma_t &= \int |f(k,\theta,\phi)|^2 d\Omega, \\
&= \int |\frac{1}{2ik}\sum_{l=0}^{\infty}(2l+1)(e^{2i\delta_l(k)}-1)P_l(\cos\theta)|^2 d\Omega, \\
&= 2\pi \int_{\theta=0}^{\theta=2\pi} \frac{1}{k^2}\sum_{l=0}^{\infty}\sum_{l'=0}^{\infty}(2l+1)(2l'+1)e^{i(\delta_l(k)-\delta_{l'}(k))} \\
&\qquad \times \sin\delta_l(k)\sin\delta_{l'}(k)P_l(\cos\theta)P_{l'}(\cos\theta)\sin\theta d\theta.
\end{aligned}
\tag{2.76}
$$

We use the orthogonality of the Legendre polynomials

$$\int_{\cos\theta=-1}^{\cos\theta=1} P_l(\cos\theta)P_{l'}(\cos\theta)d\cos\theta = \frac{2}{2l+1}\delta_{ll'}. \tag{2.77}$$

By doing the integration inside the summation, we arrive at the well-known expression

$$\sigma_t(k) = \frac{4\pi}{k^2}\sum_{l=0}^{\infty}(2l+1)\sin^2\delta_l(k) = \sum_{l=0}^{\infty}\sigma_l(k), \tag{2.78}$$

where

$$\sigma_l(k) = \frac{4\pi}{k^2}(2l+1)\sin^2\delta_l(k) \tag{2.79}$$

is the scattering cross section for individual scattering channel for each l. The total cross section is simply the sum of the independent contributions from each scattering channel.

2.4 Charge Transfer Scattering Cross Section

We now turn our attention to the charge transfer collision. Recall that the reaction can be written as

$$A^+ + B \to A + B^+. \tag{2.80}$$

We keep the label A and B to keep them distinguishable. From our discussion of the molecular orbitals in the previous sections, let us assume that there are only two solutions to the Schrödinger equation of the system (the so-called two-state approximation [11]): The wave function $\Psi_g(r)$, corresponding to the potential of the Σ_g^+

state; and $\Psi_u(r)$, corresponding to the potential of the Σ_u^+ state.

After we solve the scattering problems of these two states, we arrive at the asymptotic form similar to what we saw before, only now we have to write them in terms of tensor product of the scattered "gerade" and "ungerade" waves and the two "attached electron" states $\psi(r_A)$ and $\psi(r_B)$ given in (2.29) and (2.30):

$$\begin{aligned}
\Phi_g(r) &\rightarrow \left(e^{i\vec{k}\cdot\vec{r}} + f_g(k,\theta)\frac{e^{ikr}}{r}\right) \otimes \frac{1}{\sqrt{2}}\{\psi(r_A) + \psi(r_B)\} \\
\Phi_u(r) &\rightarrow \left(e^{i\vec{k}\cdot\vec{r}} + f_u(k,\theta)\frac{e^{ikr}}{r}\right) \otimes \frac{1}{\sqrt{2}}\{\psi(r_A) - \psi(r_B)\}.
\end{aligned} \tag{2.81}$$

If the electron is attached to the nucleus A initially (or to have the incoming wave purely $\psi(r_A)$), the wave function, $\psi(r)$, that we have to construct from (2.81) is

$$\begin{aligned}
\psi(r) &= \frac{1}{\sqrt{2}}(\Phi_g(r) + \Phi_u(r)), \\
&\rightarrow \frac{1}{2}\psi(r_A)e^{i\vec{k}\cdot\vec{r}} + \frac{e^{ikr}}{r}\frac{1}{2}\{(f_g(k,\theta) + f_u(k,\theta))\,\psi(r_A) + \\
&\qquad (f_g(k,\theta) - f_u(k,\theta))\psi(r_B)\}.
\end{aligned} \tag{2.82}$$

The charge transfer scattering amplitude is what reads in front of the term $\psi(r_B)$ because it is when the electron is attached to the nucleus B after collisions. We now examine the charge transfer scattering amplitude

$$\begin{aligned}
g(k,\theta) &= \frac{1}{2}(f_g(k,\theta) - f_u(k,\theta)) \\
&= \frac{1}{4ik^2}\sum_{l=0}^{\infty}(2l+1)P_l(\cos\theta)(e^{2i\delta_{l,g}(k)} - e^{2i\delta_{l,u}(k)}) \\
&= \frac{1}{4ik^2}\sum_{l=0}^{\infty}(2l+1)P_l(\cos\theta)(e^{2i\delta_{l,g}(k)} - e^{2i\delta_{l,u}(k)})\left(\frac{e^{-i(\delta_{l,g}(k)+\delta_{l,u}(k))}}{e^{-i(\delta_{l,g}(k)+\delta_{l,u}(k))}}\right) \\
&= \frac{1}{4ik^2}\sum_{l=0}^{\infty}(2l+1)P_l(\cos\theta)\frac{(e^{i(\delta_{l,g}(k)-\delta_{l,u}(k))} - e^{-i(\delta_{l,g}(k)-\delta_{l,u}(k)})}{(e^{-i(\delta_{l,g}(k)+\delta_{l,u}(k))})} \\
&= \frac{1}{2k^2}\sum_{l=0}^{\infty}(2l+1)P_l(\cos\theta)\sin(\delta_{g,l}(k) - \delta_{u,l}(k))e^{i(\delta_{l,g}(k)+\delta_{l,u}(k))}.
\end{aligned} \tag{2.83}$$

We can then calculate the charge transfer cross section in the same way as what we did in (2.76) and (2.77). The result is

$$\sigma_{\text{ch}} = \int |g(k,\theta)|^2 d\Omega = \frac{\pi}{k^2}\sum_{l=0}^{\infty}(2l+1)\sin^2\left(\delta_{g,l}(k) - \delta_{u,l}(k)\right). \tag{2.84}$$

2.4.1 Low Collisional Energy: Langevin Regime

To calculate the charge transfer cross section using (2.84), it is crucial to understand the behavior of $\sin^2(\delta_{g,l} - \delta_{u,l})$ at various collisional energies. Mott and Massey [11] suggest that there exists a value l_{max} such that the quantity $\sin^2(\delta_{g,l} - \delta_{u,l})$ oscillates rapidly between 0 and 1 for $l < l_{\text{max}}$. In this region it is reasonable to replace $\sin^2(\delta_{g,l} - \delta_{u,l})$ by simply 1/2. In the region where the collisional energy is low enough, we can ignore the contribution from $l > l_{\text{max}}$. Now the charge transfer cross section is given by

$$\sigma_{\text{ch}} = \frac{\pi}{k^2}\sum_{l=0}^{l_{\text{max}}}(2l+1)\frac{1}{2} = \frac{\pi}{2k^2}(l_{\text{max}}+1)^2. \tag{2.85}$$

Now the maximum angular momentum can be given by the classical angular momentum with the critical impact parameter given in (2.20). We have

$$l_{\text{max}} + 1 \simeq l_{\text{max}} \simeq \mu v_i b_0. \tag{2.86}$$

Recalling that $k = \sqrt{2\mu E}$, we obtain

$$\sigma_{\text{ch}} = \frac{1}{2}\pi b_0^2 = \frac{\sigma_{\text{Langevin}}}{2}. \tag{2.87}$$

Comparing with the classical result in (2.22), the probability of charge transfer, p_c, is 1/2. This is an expected result since for identical or nearly identical atom and ion, the electron cannot tell them apart and there is 50% chance of choosing to be bounded onto one of the two sites.

2.4.2 High Collisional Energy

The contribution from $l > l_{\text{max}}$ will become more important at higher collisional energy because, as we discussed in the previous section, the trajectories which are not spiral also contribute to the charge transfer cross section through the tunneling of an electron. Mott and Massey [11] point out that in the region where $l > l_{\text{max}}$, the value of $(\delta_{g,l} - \delta_{u,l})$ is small and $\sin^2(\delta_{g,l} - \delta_{u,l}) \sim (\delta_{g,l} - \delta_{u,l})^2$. With large value of l, we can write (2.84) to be

$$\sigma_{\mathrm{ch}} = \frac{\pi}{k^2}\left(\int_0^L (2l+1)\sin^2(\delta_{g,l}-\delta_{u,l})dl + \int_L^\infty (2l+1)(\delta_{g,l}-\delta_{u,l})^2 dl\right), \tag{2.88}$$

where we have written $L = l_{\max}$. We now use the result of semiclassical approximation, and the phase shift can be written as

$$(\delta_{g,l}-\delta_{u,l}) \simeq -\mu \int_{\frac{(l+1/2)}{k}}^{\infty} \frac{V_{\mathrm{exc.}}(r)}{(k^2 - \frac{(l+1/2)^2}{r^2})^{1/2}} dr \tag{2.89}$$

where $V_{\mathrm{exc.}}(r)$ is the exchange potential as demonstrated in (2.34)[15]. Generally, $V_{\mathrm{exc.}}(r)$ is given by

$$V_{\mathrm{exc.}}(r) = Are^{-\lambda r}, \tag{2.90}$$

where A and λ are constants.[7] With this form of exchange potential, and writing the impact parameter as $b = (l+\frac{1}{2})/k$, the integral yields

$$(\delta_{g,l}-\delta_{u,l}) = -\frac{Ab^2\mu}{k}\left(K_0(\lambda b) + \frac{K_1(\lambda b)}{\lambda b}\right), \tag{2.91}$$

where K_0 and K_1 are the modified Bessel functions of the second kind [16]. We can use the asymptotic forms of the modified Bessel functions [17],

$$K_{0,1}(\lambda b) \sim \sqrt{\frac{\pi}{2\lambda b}}e^{-\lambda b}, \tag{2.92}$$

and then write

$$(\delta_{g,l}-\delta_{u,l}) = -\frac{Ab^2\mu}{k}\sqrt{\frac{\pi}{2\lambda b}}e^{-\lambda b}(1+\frac{1}{\lambda b}). \tag{2.93}$$

Let us look at the plot of $\sin^2(\delta_{g,l}-\delta_{u,l})$ against b as shown in Figure 2-6. The region where $\sin^2(\delta_{g,l}-\delta_{u,l})$ oscillates rapidly corresponds to the case where the classical trajectory is spiral (as in Figure 2-3). The value of B, which is chosen to be the point where we divide the two regions, is, however, somewhat arbitrary. In our case, we will set B to be the largest b such that $\sin^2(\delta_{g,l}-\delta_{u,l}) = 1/2$, i.e., $|\delta_{g,l}-\delta_{u,l}| = \pi/4$.

---

[7] The form of $V_{\mathrm{exc.}}(r) = Ce^{-\lambda r}$ is also possible and will give the same asymptotic form for charge transfer cross section [16].

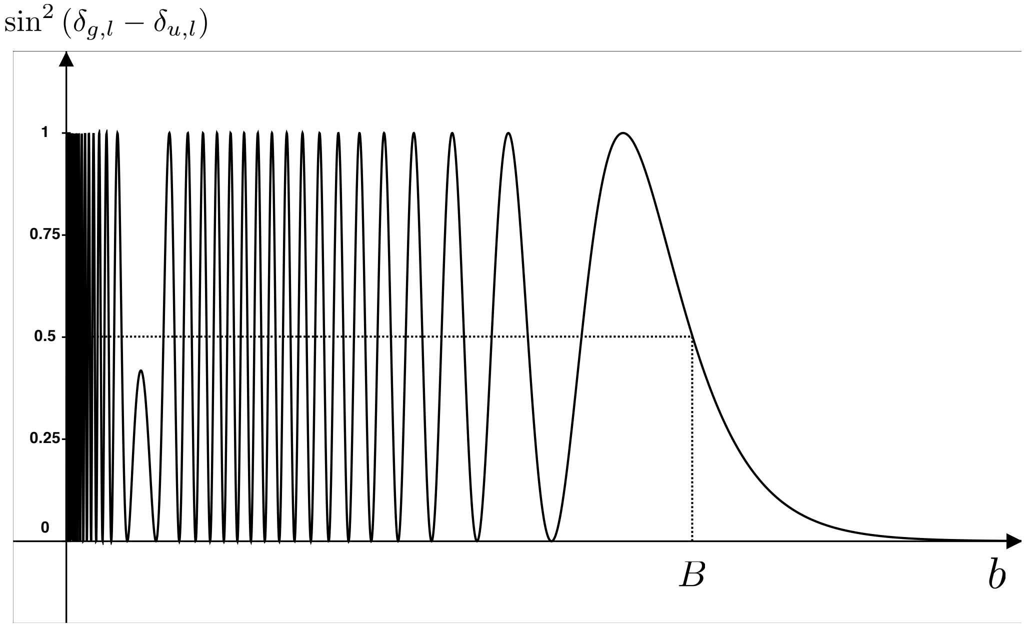

Figure 2-6: Plot of $\sin^2(\delta_{g,l} - \delta_{u,l})$ against b. For $0 < b < B$, the value of $\sin^2(\delta_{g,l} - \delta_{u,l})$ oscillates rapidly between 0 and 1, so we can use the average value of 1/2. For $b > B$, we use $\sin^2(\delta_{g,l} - \delta_{u,l}) \sim (\delta_{g,l} - \delta_{u,l})^2$ and carry on the integration given in (2.88).

From (2.93), we get

$$\frac{AB^2\mu}{k}\sqrt{\frac{\pi}{2\lambda B}}e^{-\lambda B}(1+\frac{1}{\lambda B})=\frac{\pi}{4}. \tag{2.94}$$

By using $B=(L+\frac{1}{2})/k$ and (2.93), the integral in (2.88) becomes

$$\sigma_{\mathrm{ch}}=\frac{1}{2}\pi B^2+\frac{\pi}{k^2}\left(\frac{A^2\mu^2\pi}{4\lambda^6}\left(7+14\lambda B+14(\lambda B)^2+8(\lambda B)^3+2(\lambda B)^4\right)e^{-2\lambda B}\right). \tag{2.95}$$

Using (2.94) and keeping only the leading terms, we can write

$$\sigma_{\mathrm{ch}}=\frac{1}{2}\pi B^2+\frac{\pi^3 B}{16\lambda}=\frac{\pi}{2}\left((B+\frac{\pi^2}{16\lambda})^2-(\frac{\pi^2}{16\lambda})^2\right). \tag{2.96}$$

To solve for B, we can approximate (2.94) by rewriting the expression to be

$$\frac{A^2B^3\mu^2\pi}{k^2\lambda}e^{-2\lambda B}=\frac{\pi^2}{8}. \tag{2.97}$$

Since the dominating fast-varying term is $e^{-2\lambda B}$, we can replace B in front of the exponential term by a fixed average value which we will denote by $\bar{B}$ [10].[8] We can now, with $k=\sqrt{2\mu E_c}$, write

$$B=-\frac{1}{2\lambda}\left(\ln E_c+\ln\frac{\lambda\pi}{4A^2\bar{B}^3\mu}\right). \tag{2.98}$$

With this and (2.96), we arrive at the expression

$$\sigma_{\mathrm{ch}}\simeq\frac{\pi}{8\lambda^2}\left(\left(\ln E_c+\ln\frac{\lambda\pi}{4A^2\bar{B}^3\mu}-\frac{\pi^2}{16\lambda}\right)^2-(\frac{\pi^2}{8})^2\right). \tag{2.99}$$

To a very good approximation, we can rewrite the expression in the general form

$$\sigma_{\mathrm{ch}}\simeq(a\ln E_c+b)^2, \tag{2.100}$$

as in (2.24). The plots of charge transfer cross section against collisional energy is shown in Figure 2-7. The cross section can be divided into two regions: the Langevin cross section dominated and $(a\ln E_c+b)^2$ dominated. The plot uses the parameters

---

[8] $\bar{B}$ is the average value of B over different values of k.

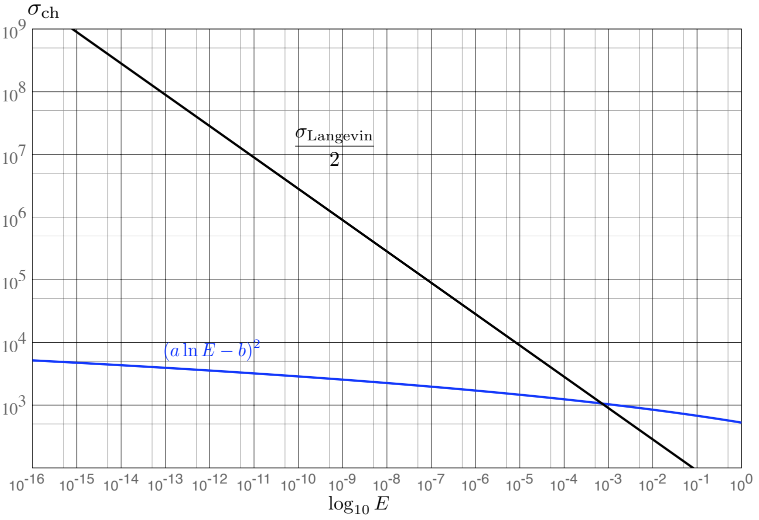

Figure 2-7: Charge transfer cross section against collisional energy in atomic units from two contributions: Langevin cross section contribution (black) and the long range $re^{-\lambda r}$ potential (blue).

given for sodium in [15], where the exact calculation of the charge transfer cross section for Na^++ Na is done.

2.5 Ion Loss Rate from Charge Transfer Collisions

Assume that we have a system consisting of $^{172}\mathrm{Yb}^+$ and $^{174}\mathrm{Yb}$. Despite the fact that they are different isotopes, we will assume that they are nearly identical and our assumptions so far are still valid. In other words, when we discuss hydrogen molecular ion, we assume that the two nuclei are “similar” but “distinguishable” particles by imposing the “gerade” and “ungerade” symmetries but labeling the two nuclei by A and B. This is still justified in our discussion of $^{172}\mathrm{Yb}^+$ and $^{174}\mathrm{Yb}$ since the isotope effect has a very small effect on electronic structure.

Suppose we set up the experiment such that the ions in the confinement will be lost if charge transfer collisions happen. What we would like to calculate is the total loss rate of the ions. In the following chapters we will see that the ion density is a lot lower than atomic density, and atomic motion is a lot slower than ion motion. Let us denote n_a to be the density of $^{174}\mathrm{Yb}$ atoms. The charge transfer cross section is $\sigma_{\rm ch}$.

In time Δt, an ion with relative velocity v_i will sweep a volume

$$\Delta V = \sigma_{\text{ch}} v_i \Delta t. \tag{2.101}$$

During this time, an ion will encounter N_a atoms, where

$$N_a = n_a \Delta V = n_a \sigma_{\text{ch}} v_i \Delta t. \tag{2.102}$$

Per unit time, an ion will suffer Γ scattering events. We then have

$$\Gamma = n_a \sigma_{\text{ch}} v_i. \tag{2.103}$$

For each charge transfer collision event, our experimental setup is designed in a way that one $^{172}\text{Yb}^+$ ion is removed from the ion cloud. If we have N ions at any time t, then our rate equation is

$$\frac{dN}{dt} = -\Gamma N = -n_a \sigma_{\text{ch}} v_i N. \tag{2.104}$$

This is clear that the population of ions, N, will be described by an exponential decay. Generally,

$$N(t) = N(0)e^{-\Gamma t} = N(0)e^{-n_a \sigma_{\text{ch}} v_i t}. \tag{2.105}$$

If we are in the region where the charge transfer cross section is described by the Langevin cross section, then we have, for our decay constant,

$$\begin{aligned}
\Gamma &= n_a \sigma_{\text{ch}} v_i \\
&= \frac{1}{2} n_a \pi b_0^2 v_i \\
&= \frac{1}{2} n_a \pi v_i \sqrt{\frac{8k\alpha}{v_i^2 \mu}} \\
&= \frac{1}{2} n_a \pi \sqrt{\frac{4\alpha}{\mu}},
\end{aligned} \tag{2.106}$$

where we have used the fact that $k = 1/2$ in atomic units. It is important to point out that the v_i dependence in the decay constant vanishes. Now the polarizability, α, can be measured directly through the decay constant provided that we know the atomic density, n_a.

In the actual experiment, however, we do not have a constant atomic nor ion density. The atomic and ion densities are given by the profiles specified in three-dimensional space. We also have different overlaps between the atoms and ions. In this case, we calculate the average atomic density seen by a single ion using

$$\langle n_a \rangle = \frac{\int_{-\infty}^{\infty} n_i(\vec{r}) n_a(\vec{r}) dV}{\int_{-\infty}^{\infty} n_i(\vec{r}) dV}, \tag{2.107}$$

where $n_i(\vec{r})$ and $n_a(\vec{r})$ are the density profile of ions and atoms, respectively. Normally, we can model both ion and atomic density to be the Gaussian function. Actual details about the estimation of atomic density will be done in the later chapter.

Chapter 3

Laser Cooling and Trapping of Neutral Atoms

To perform atom-ion collision experiments at low temperature, it is crucial to have a way to confine atoms in a finite spatial region and keep them at low temperature. This is possible through the method of laser cooling and the use of a magneto-optical trap (MOT), which combines photon-atom interaction with external magnetic fields and creates a trapping potential. In this chapter we will present a theory behind laser cooling and MOT. The experimental setup for the MOT in our experiment for ytterbium will follow. In this chapter we shall again work in atomic units unless noted.

3.1 Light Force on Two-Level Atoms

In our discussions we can treat any Yb atom to be a two-level atom because the light that we use to drive the transition is very close to the resonance frequency and we can ignore the contribution from other energy levels.

3.1.1 Radiation Pressure

Radiation pressure on an atom can be understood easily by considering a two-level atom. Let us denote the ground state of the atom to be $|g\rangle$ and the excited state to be $|e\rangle$. The energy splitting between the two levels is given by ω_0. The idea behind radiation pressure is that an atom will absorb a photon when the frequency of a photon, ω, is very close or equal to ω_0 in the atomic frame. Since a photon carries momentum of ω/c where c is the speed of light in vacuum, conservation of momentum requires that the momentum of an atom changes in the direction of the propagation of a photon. An atom will eventually emit a photon and be back to its ground state again, but this time there is no preferred emitting direction so the net momentum change will be in the photon direction before it is being absorbed by an atom. The following treatment is a general one suggested by [18].

Consider an interaction of a two-level atom with a plane monochromatic wave. The electric field is given by

$$\vec{E}(\vec{r},t) = \vec{E}_0 e^{-i(\vec{k}\cdot\vec{r}-\omega_L)t}, \tag{3.1}$$

where ω_L is the frequency of the driving electric field. The Hamiltonian of the system can be written as

$$\hat{H} = \left(\begin{array}{cc} \omega_0 & -\vec{d}\cdot\vec{E}(\vec{r},t) \\ \vec{d}\cdot\vec{E}^*(\vec{r},t) & 0 \end{array} \right), \tag{3.2}$$

where $\vec{d}$ is the matrix element of a dipole operator, $\hat{D}$, between $|e\rangle$ and $|g\rangle$, namely,

$$\vec{d} = \langle e|\, \hat{D}\, |g\rangle = \langle g|\, \hat{D}\, |e\rangle^* . \tag{3.3}$$

We can solve the time evolution of the density matrix operator, $\hat{\rho}$, using

$$i\frac{d\hat{\rho}}{dt} = [\hat{H},\hat{\rho}], \tag{3.4}$$

where

$$\hat{\rho} = \left(\begin{array}{cc} \rho_{ee} & \rho_{eg} \\ \rho_{ge} & \rho_{gg} \end{array} \right). \tag{3.5}$$

We then obtain

$$\frac{d\rho_{ee}}{dt} = i\vec{d}\cdot\vec{E}_0 e^{-i(\vec{k}\cdot\vec{r}-\omega_L)t}\rho_{ge} - i\vec{d}\cdot\vec{E}_0 e^{i(\vec{k}\cdot\vec{r}-\omega_L)t}\rho_{eg}, \tag{3.6}$$

$$\frac{d\rho_{eg}}{dt} = -i\omega_0\rho_{eg} + i\vec{d}\cdot\vec{E}_0 e^{-i(\vec{k}\cdot\vec{r}-\omega_L)t}(\rho_{gg}-\rho_{ee}), \tag{3.7}$$

$$\frac{d\rho_{gg}}{dt} = -\frac{d\rho_{ee}}{dt}, \tag{3.8}$$

$$\frac{d\rho_{ge}}{dt} = \left(\frac{d\rho_{eg}}{dt}\right)^* . \tag{3.9}$$

We add the coupling to the empty modes of vacuum by simply adding the decay constant, Γ, which denotes the life time of the $|e\rangle$ state. With this modification, we arrive at the optical Bloch equation

$$\frac{d\rho_{ee}}{dt} = -\Gamma\rho_{ee} + i\vec{d}\cdot\vec{E}_0 e^{-i(\vec{k}\cdot\vec{r}-\omega_L)t}\rho_{ge} - i\vec{d}\cdot\vec{E}_0 e^{i(\vec{k}\cdot\vec{r}-\omega_L)t}\rho_{eg}, \tag{3.10}$$

$$\frac{d\rho_{eg}}{dt} = (-i\omega_0 - \frac{\Gamma}{2})\rho_{eg} + i\vec{d}\cdot\vec{E}_0 e^{-i(\vec{k}\cdot\vec{r}-\omega_L)t}(\rho_{gg} - \rho_{ee}). \tag{3.11}$$

Let us introduce the detuning parameter, $\Delta = \omega_L - \omega_0$. From these equations, we can look for the steady state of the density matrix. We will arrive at

$$\rho_{eg} = i\frac{\vec{d}\cdot\vec{E}_0 e^{-i(\vec{k}\cdot\vec{r}-\omega_L)t}/\hbar}{i\Delta + \Gamma/2}(1 - 2\rho_{ee}), \tag{3.12}$$

$$\rho_{ee} = \frac{s_0}{2(s_0+1)}, \tag{3.13}$$

where

$$s_0 = \frac{2|\vec{d}\cdot\vec{E}_0|^2}{\Delta^2 + \Gamma^2/4} \tag{3.14}$$

is the saturation parameter.

We now introduce the force operator:

$$\hat{F} = -\nabla_r \hat{H}. \tag{3.15}$$

The expectation value of this force operator in the steady state is given by

$$\begin{aligned}\vec{f} &= \mathrm{Tr}(\hat{\rho}\hat{F}),\\ &= \vec{k}\frac{\Gamma}{2}\frac{s_0}{1+s_0}.\end{aligned} \tag{3.16}$$

This force expression can be viewed as a scattering rate, $\left(\frac{\Gamma}{2}\frac{s_0}{1+s_0}\right)$, times the momentum transfer, $\vec{k}$. If an atom is moving at velocity $\vec{v}$, then the force expression will be modified according to the Doppler effect. The force is then

$$\vec{f} = \vec{k}\frac{\Gamma}{2}\frac{s(\vec{v})}{1+s(\vec{v})}, \tag{3.17}$$

where

$$s(\vec{v}) = \frac{2|\vec{d}\cdot\vec{E}_0|^2}{(\Delta - \vec{k}\cdot\vec{v})^2 + \Gamma^2/4}. \tag{3.18}$$

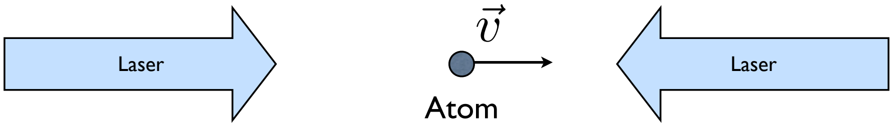

Figure 3-1: One-dimensional doppler cooling.

Note that our analysis holds as long as we are in the region where the recoil velocity is very small compared to the line width of the transition, namely,

$$\frac{k^2}{m} \ll \Gamma. \tag{3.19}$$

where m is the atomic mass.

3.1.2 Doppler Cooling

Consider now the situation in Figure 3-1 where we consider the one-dimensional case. We have counter-propagating laser beams of the same detuning, Δ. The total force on the atom is given by the interactions with the two beams

$$f(v) = k\Gamma \left(\frac{|\vec{d} \cdot \vec{E}_0|^2}{(\Delta - kv)^2 + \Gamma^2/4} - \frac{|\vec{d} \cdot \vec{E}_0|^2}{(\Delta + kv)^2 + \Gamma^2/4} \right), \tag{3.20}$$

with the fact that the saturation parameter is a lot less than one, $s \ll 1$. At low velocity, we can approximate the force expression to be

$$f(v) = -\gamma v = -\left(\frac{-2k^2 s_0 \Delta\Gamma}{\Delta^2 + \Gamma^2/4} \right) v. \tag{3.21}$$

The force is a damping force if Δ is negative. This is the case where we have a red-detuned laser. This damping force will result in cooling of the atoms. This is the so-called Doppler cooling since it arises from the Doppler effect.

Despite the Doppler cooling, the atoms will receive two random momentum kicks of $|\vec{p}| = |\vec{k}|$ each time the scattering event happens: one from absorption and another from emission. The net change in the energy due to this heating mechanism is given by

$$\frac{d}{dt}\langle E\rangle_{\text{heat}} \simeq 2 \times \frac{k^2}{m}\frac{\Gamma}{2}\frac{s_0}{1+s_0}, \tag{3.22}$$

where the "2" in front came from the fact that we have two laser beams and m is the atomic mass. Now the cooling rate is simply given by the power done by the cooling force

$$\begin{aligned}\frac{d}{dt}\langle E\rangle_{\text{cool}} &= f \cdot v \\ &\simeq \left(\frac{-2k^2 s_0 \Delta\Gamma}{\Delta^2 + \Gamma^2/4}\right) v^2. \end{aligned} \tag{3.23}$$

At equilibrium, the heating rate balance the cooling rate. We then have

$$\begin{aligned}\frac{d}{dt}\langle E\rangle_{\text{cool}} &= \frac{d}{dt}\langle E\rangle_{\text{heat}} \\ \left(\frac{-2k^2 s_0 \Delta\Gamma}{\Delta^2 + \Gamma^2/4}\right) v^2 &= 2\frac{k^2}{m}\frac{\Gamma}{2}\frac{s_0}{1+s_0}.\end{aligned}$$

With $s_0 \ll 1$, we arrive at

$$\frac{1}{2}mv^2 = -\frac{1}{4}\frac{\Delta^2 + \Gamma^2/4}{\Delta}. \tag{3.24}$$

The detuning Δ that will minimize this expression is $\Delta = -\Gamma/2$. We then have

$$\frac{1}{2}mv^2 = \frac{\Gamma}{4}. \tag{3.25}$$

This is the lowest kinetic energy of atoms under the Doppler cooling. In our case, we have the relationships between the mean kinetic energy and temperature as

$$\langle E_{\text{k}}\rangle = \frac{1}{2}mv^2 = \frac{1}{2}k_B T. \tag{3.26}$$

We then define the Doppler limit temperature to be

$$T_D = \frac{\Gamma}{2k_B} = \frac{\Gamma\hbar}{2k_B}\ (\text{SI})\ . \tag{3.27}$$

Note that the Doppler limit depends only on the line width of the transition. For

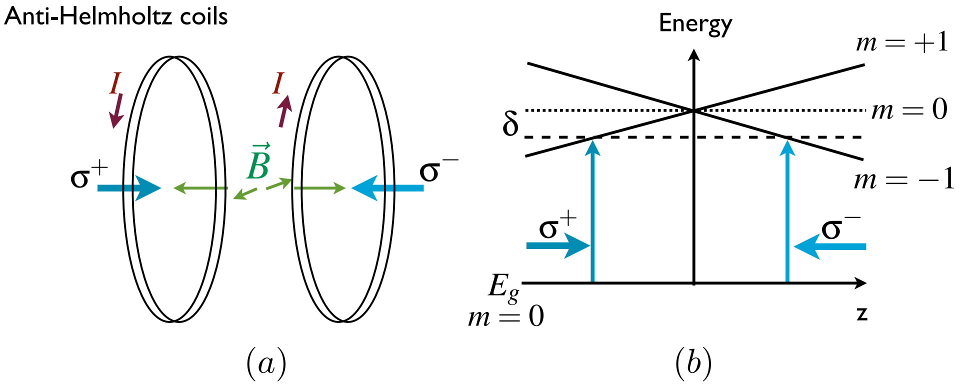

Figure 3-2: General configuration of magneto-optical trap.

${}^1S_0 \to {}^1P_1$ transition of Yb, the line width, Γ, is $2\pi \times 28$ MHz giving the Doppler temperature to be $T_D = 690\mu$K [19].

3.2 Magneto-Optical Trap

The light force expression (3.21) is a frictional force. Hence, it is not restorative. The mechanism of the magneto-optical trap is to apply a magnetic field gradient in a way that the interaction between atoms and magnetic field will push them back to an equilibrium point.

Without loss of generality, we now consider the problem to be one-dimensional. Suppose we have a magnetic field that is linear in z, namely,

$$\vec{B} = zB'_z\hat{e}_z. \tag{3.28}$$

where B'_z is the field gradient in the z direction. This magnetic field configuration can be generated by a pair of anti-Helmholtz coils. The quantitative analysis of the magnetic field produced by the anti-Helmholtz coils can be found in [3]. The ${}^1P_1$ level will split due to its magnetic quantum number. The splitting depends linearly on $|\vec{B}|$. Figure 3-2 shows how the energy level depends on the position z. Now imagine that we have a right circularly polarized (σ^+) light coming from the left, and a left circularly polarized light (σ^-) coming from the right. Because each photon carries angular momentum of 1 for σ^+ light and -1 for σ^- light, the atom displaced to the left (relative to $z = 0$) will preferentially absorb the σ^+ light since the scattering rate from σ^- light is a lot smaller. The light radiation pressure will push the atom back to the origin. If the atom is displaced to the right, it will preferentially absorb σ^- light. Again, the light radiation pressure will push the atom back to the origin.

To view this quantitatively, let us look at the position dependence of the detuning of the laser. In Figure 3-2, at $z = 0$ assuming that the atom is at rest, the only detuning is from the laser detuning, Δ. Because of the Zeeman shift, the additional detuning, $\delta(z)$, is from the splitting of the energy level between $m = \pm 1$ states and $m = 0$ state. We can write

$$\pm\delta(z) = \pm\frac{g\mu_B B(z)}{\hbar}\ \text{(SI)}\ = \pm\frac{gB(z)}{2}\ \text{(a.u.)}\ , \tag{3.29}$$

where μ_B is the Bohr magneton and g is the Landé g-factor [20]. The sign in front of the expression depends on whether the light is σ^+ or σ^-. Now we can write the light force analogous to (3.20),

$$f_B(z) = k\Gamma\left(\frac{|\vec{d}\cdot\vec{E}_0|^2}{(\Delta+\delta(z))^2+\Gamma^2/4} - \frac{|\vec{d}\cdot\vec{E}_0|^2}{(\Delta-\delta(z))^2+\Gamma^2/4}\right). \tag{3.30}$$

With the same approximation we did before, we have

$$f_B(z) = -k\Gamma\left(\frac{2s_0\Delta\delta(z)}{\Delta^2+\Gamma^2/4}\right). \tag{3.31}$$

We now substitute $\delta(z)$ from (3.29) and get

$$\begin{aligned} f_B(z) &= -k\Gamma\left(\frac{2s_0\Delta(gB(z)/2)}{\Delta^2+\Gamma^2/4}\right) \\ &= -k\Gamma\left(\frac{s_0\Delta g B'_z}{\Delta^2+\Gamma^2/4}\right)z. \end{aligned} \tag{3.32}$$

Clearly we have here a restorative force that will push back the atoms towards the origin. Our analysis here can be extended to three-dimensional case and it is straightforward since all directions are independent of each other.

Chapter 4

Trapping of Ions

In this chapter we turn our attention to the trapping of ions. Because ions are charged, they can be confined in a spatial region using the Coulombic interaction. Although Laplace's equation prevents us from having a trapping potential in free space with only electrostatic interactions, we will see that modulating electric fields at radio frequency (rf) creates a trapping pseudopotential, in which we can successfully tightly confine ions in free space. The theory of the linear rf-Paul trap will be presented. Then the discussion of micromotion energy, which is important in our collision experiment, will follow. In the last section we will show our planar trap geometry, the experimental procedure and the results of ions produced and trapped.

4.1 General Trapping Mechanism

The idea behind ion trapping is the generation of a pseudopotential from external perturbation. One classic example is the so-called Kapitsa pendulum [21]. Imagine a charged bead on a circular ring as in Figure 4-1. Normally, the motion of the bead will be that of a simple pendulum. If we apply a small external electric field at an appropriate frequency, amplitude and phase, then it can be shown that the point on the top of the ring is also a stable point. The idea of using these principles to trap ions was proposed by Wolfgang Paul in 1950s.[1] In 1989, Wolfgang Paul and Hans G. Dehmelt were awarded the Nobel Prize in Physics from their works on ion traps.[2]

---

[1] Hans G. Dehmelt was involved in the so-called Penning trap where the trapping mechanism is different from the Paul trap.

[2] Norman Foster Ramsey was also a co-recipient for his work on atomic clock and the so-called Ramsey method.

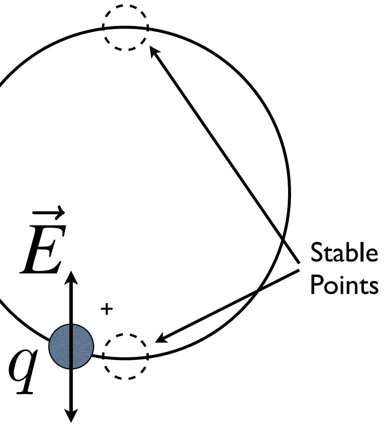

Figure 4-1: Kapitsa pendulum. If we choose the phase and frequency of $\vec{E}$ right, then we will have another stable point on the top of the ring.

4.1.1 Linear Paul Trap

The so-called Paul trap has many configurations. Although what we use in the experiment is a planar three-rod trap, it is more illuminating to discuss the usual four-rod trap in this section. Once we have the basic idea of its mechanism, then the three-rod trap can be understood in the same manner.

A usual four-rod trap is shown in Figure 4-2 (*a*). We apply an alternating rf potential in a form of

$$V(t) = \pm(V_0 + V_1 \cos(\Omega t)) \tag{4.1}$$

where V_0 is a DC-offset voltage, V_1 is the rf amplitude and Ω is the driving rf frequency. Because the rods' shape approximates closely the quadrupole equipotential surface, it can be shown that the potential near the trap center is

$$\Phi(x, y, t) = (V_0 + V_1 \cos(\Omega t))\frac{x^2 - y^2}{R^2}, \tag{4.2}$$

where we use the coordinate system shown in Figure 4-2 (*b*).

The endcaps held at potential U_0 will create a static potential near the center of the trap given by

$$U(x, y, z) = \frac{\kappa U_0}{Z_0^2}[z^2 - \frac{1}{2}(x^2 + y^2)], \tag{4.3}$$

where κ is a geometrical factor, Z_0 is the distance between the endcaps or the length of the rods [22]. Combining these two potentials at the center of the trap, the electric

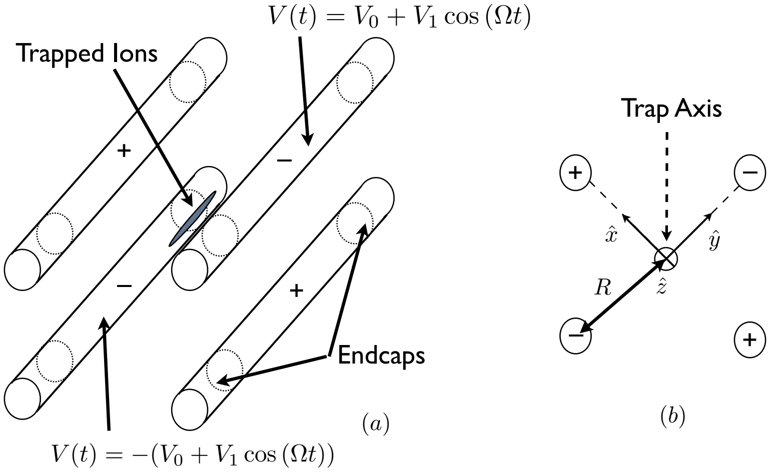

Figure 4-2: Four-rod Paul trap. (a) Little cylinder at the end of each rod is the place where we apply the endcap potential to confine the ions axially. (b) The coordinate system used in our analysis.

field can be calculated by taking the gradient of the sum of the potential. We will find

$$\vec{E}(x, y, z, t) = -2V_1 \frac{x\hat{x} - y\hat{y}}{R^2} \cos(\Omega t) - \frac{\kappa U_0}{Z_0^2}[2z\hat{z} - x\hat{x} - y\hat{y}]. \tag{4.4}$$

Suppose we have a single ion at the trap center with mass m and charge Q. We will have a set of equation of motion in the following form:

$$\ddot{u}_i + [a_i + 2q_i \cos(\Omega t)] \frac{\Omega^2}{4} u_i = 0, \tag{4.5}$$

where

$$\vec{u} = u_x\hat{x} + u_y\hat{y} + u_z\hat{z} \tag{4.6}$$

is the position vector of the ion measured from the center of the trap, and

$$a_x = a_y = -\frac{1}{2}a_z = -\frac{4Q\kappa U_0}{mZ_0^2\Omega^2} \tag{4.7}$$

and

$$q_x = -q_y = \frac{4QV_1}{mR^2\Omega^2}, \tag{4.8}$$

$$q_z = 0. \tag{4.9}$$

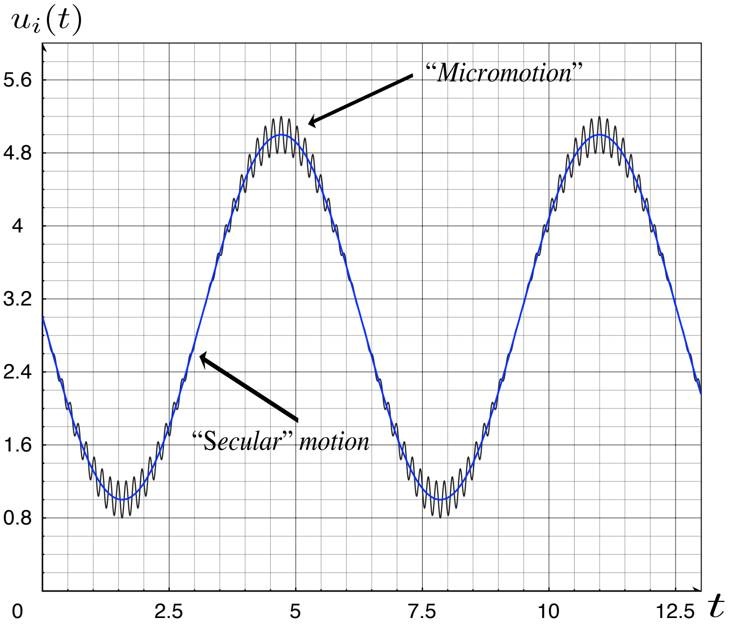

Figure 4-3: Sample trajectory of the ion in the trap plotted in arbitrary units. Note that it can be separated into the the fast "micromotion" and the slow "secular" motion. For this plot $\omega_i/\Omega_i = 0.03$.

The differential equation (4.5) is the so-called Mathieu equation, where the stability of the solutions depends on a_i and q_i. The first stability region requires $q_i < 0.908$ [3]. However, in our case, we will assume that $|a_i| \ll 0$ and $|q_i| \ll 0$, and these conditions will ensure that we have stable solutions for the Mathieu equation. The first-order solution is given by

$$u_i(t) \sim u_{0i} \cos(\omega_i t + \eta_i) \left(1 + \frac{q_i}{2} \cos(\Omega t)\right), \tag{4.10}$$

where ω_i is a slower angular frequency which depends on Ω, a_i and q_i. Typically in our experiment, ω_i/Ω will be around 0.1 or lower [2]. Figure 4-3 shows the plot of $u_i(t)$ in some sample a_i and q_i parameters. The trajectory of the ion can be divided into the fast "micromotion" and the slow "secular" motion. We then call ω_i to be the secular frequency. Note that for z-axis, since $q_z = 0$, we do not have any driven micromotion in this direction.

To derive a general secular pseudopotential, let us look at (4.5) again. We can write the position of the ion to be the sum of the secular motion and the micromotion, i.e.,

$$u_i = u_{\text{micro}} + u_{\text{secular}}. \tag{4.11}$$

Now (4.5) becomes

$$\ddot{u}_{\text{micro}} + \ddot{u}_{\text{secular}} = -[a_i + 2q_i \cos(\Omega t)]\frac{\Omega^2}{4}(u_{\text{micro}} + u_{\text{secular}}). \tag{4.12}$$

Since $\ddot{u}_{\text{micro}} \gg \ddot{u}_{\text{secular}}$ and $u_{\text{micro}} \ll u_{\text{secular}}$ because of the difference in scale, we have

$$\ddot{u}_{\text{micro}} = -[a_i + 2q_i \cos(\Omega t)]\frac{\Omega^2}{4}u_{\text{secular}}. \tag{4.13}$$

We can now use the fact that the micromotion is a driven motion, i.e., $\ddot{u}_{\text{micro}} = -\Omega^2 u_{\text{micro}}$, and arrive at

$$\Omega^2 u_{\text{micro}} = [a_i + 2q_i \cos(\Omega t)]\frac{\Omega^2}{4}u_{\text{secular}}. \tag{4.14}$$

Substituting this expression back into (4.12) yields

$$\ddot{u}_{\text{secular}} = -\left(a_i + 2q_i \cos(\Omega t)\right)^2 \frac{\Omega^2}{16}u_{\text{secular}}. \tag{4.15}$$

Using $\langle \cos(\Omega t) \rangle = 0$ and $\langle \cos^2(\Omega t) \rangle = 1/2$, we have

$$\ddot{u}_{\text{secular}} = -\left(a_i^2 + 2q_i^2\right)\frac{\Omega^2}{16}u_{\text{secular}} = -\omega_i^2 u_{\text{secular}}. \tag{4.16}$$

The secular motion is harmonic with an angular frequency of

$$\omega_i = \frac{\Omega}{4}\sqrt{a_i^2 + 2q_i^2}. \tag{4.17}$$

The trap depth, D, can be defined as the energy required for an ion at rest at the center of the trap to escape the trap [20]. This is simply given by

$$D = \frac{1}{2}\omega_i^2 m R^2. \tag{4.18}$$

4.1.2 Three-Rod Paul Trap

A four-rod trap limits our optical access to the trapped ions in the center, making it harder to combine this configuration with a MOT. If we want to gain more accessibility, or more space for the ions to move around, it is more convenient to use instead a three-rod configuration.

Basically the three-rod planar trap is constructed by pulling one of the four rods in the four-rod trap far away and flatten the remaining three rods. The analysis of a three-rod trap can be found in [23]. The analysis is complicated and the numerical calculation is done using the Boundary Element Method [2]. The simulated potential is shown in Figure 4-4. We made a trap by printing the trace on a low-loss Roger 4350 substrate and cut away for better optically accessibility. The trap is shown in Figure 4-5. The complete description of the trap used in our experiment can be found in [3, 20, 2]. We drive the trap at a rf frequency of 850 kHz. The center electrode potential and the outer electrodes potential are at 540 V (1080 $V_{\text{p-p}}$) and -340 V (680 $V_{\text{p-p}}$), respectively [2]. The distance between each electrode is 3 mm. With these parameters, we have a trap with measured secular frequency of 70 kHz and a calculated trap depth of 0.16 eV. The surrounding smaller electrodes are for trap compensation. We will see in the next section how these electrodes play an important role in changing the micromotion energy of the ions.

We can deepen the trap by applying a DC bias to the rf potential to the three main electrodes. This allows us to first load the ions with a deep trap and then remove the DC bias to decrease the trap depth. With this method, we can load traps with a trap depth as small as 0.13 eV [2].

4.2 Ion Micromotion Energy

We now look at the motion of a single ion. Let us look at the motion in x and y axis. From (4.10) we can calculate the average kinetic energy over the period of the secular motion

$$\begin{aligned} E_{ki} &= \frac{1}{2}m\langle \dot{u}_i^2\rangle \\ &\simeq \frac{1}{4}mu_{0i}^2(\omega_i^2 + \frac{1}{8}q_i^2\Omega^2) \\ &\simeq \frac{1}{4}mu_{0i}^2\omega_i^2(1 + \frac{q_i^2}{q_i^2 + a_i^2/2}), \end{aligned} \tag{4.19}$$

where the first term in the last expression is the kinetic energy due to the secular motion and the second term is the kinetic energy due to the micromotion [22]. For the motion in z axis, the micromotion energy is simply zero because $q_z = 0$. Typically,

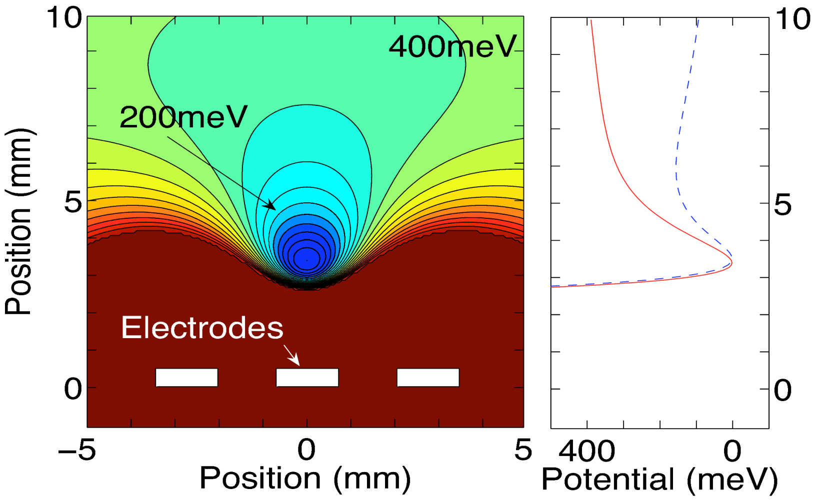

Figure 4-4: Simulated potential produced by the three-rod planar trap. Left: Contour plot of the trapping potential and the trapping point relative to the electrodes. Right: The dashed-line shows the DC unbiased trapping potential and the solid red line is when the DC biased is applied. Image reproduced from [2].

we have $|a_i| \ll q_i^2$ for $i = x, y$. We can immediately see that the radial secular energy is equal to the energy of the microtion.

The surrounding smaller electrodes that we use to compensate the trap and to axially confine the ions (as endcaps) will produce a non-zero electric field around the center of the trap. This electric field is denoted by $\vec{E}_{\mathrm{dc}}$; and the Mathieu equation in (4.5) is replaced by

$$\ddot{u}_i + [a_i + 2q_i \cos{(\Omega t)}]\frac{\Omega^2}{4}u_i = \frac{Q\vec{E}_{\mathrm{dc}} \cdot \hat{u}_i}{m}. \tag{4.20}$$

The extra term on the right hand side will displace the micromotion from the center of the trap by

$$u'_{0i} \simeq \frac{4Q\vec{E}_{\mathrm{dc}} \cdot \hat{u}_i}{m(a_i^2/4 + q_i^2/2)\Omega^2} \simeq \frac{Q\vec{E}_{\mathrm{dc}} \cdot \hat{u}_i}{m\omega_i^2}. \tag{4.21}$$

The total kinetic energy in the i direction, following the treatment by [22], is now given by

$$E_{ki} = \frac{1}{4}mu_{0i}^2\omega_i^2(1 + \frac{q_i^2}{q_i^2 + a_i^2/2}) + \frac{4}{m}\frac{Qq_i\vec{E}_{\mathrm{dc}} \cdot \hat{u}_i}{(a_i^2/2 + q_i^2)\Omega}. \tag{4.22}$$

This total ion kinetic energy is the collisional energy in atom-ion collisions, and we

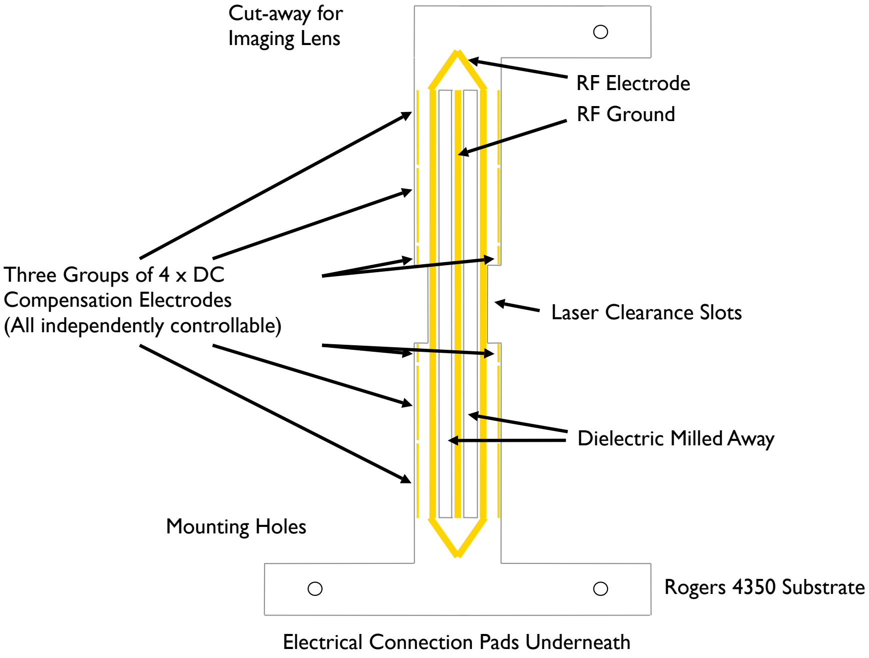

Figure 4-5: Planar trap: The three main electrodes are positioned in the center of the chips. The surrounding smaller electrodes are for trap compensation which we can use to move around the trap center and change the trap depth. Image reproduced from [3].

can adjust the collisional energy by changing the electric field around the the center of the trap. In a well compensated trap, meaning that $\vec{E}_{\rm dc} = 0$, the micromotion of the ion is minimized.

4.3 Crystallization of Ions

If the kinetic energy of the ions in the trap is low enough, the ions can form the so-called Coulombic crystal. The condition for the formation of the crystal is that the Coulomb coupling parameter,

$$\Theta = \frac{e^2}{ak_BT} > 150, \tag{4.23}$$

where a is the Wigner-Seitz radius [24]. This is where the crystal mean-field interaction is a lot larger than the thermal energy. We can estimate a by simply balancing the Coulombic force and the force produced by the harmonic potential of the trap. We have

$$\begin{aligned} F_{\rm Coulomb} &= F_{\rm harmonic} \\ -\frac{e^2}{a^2} &= -m\omega_{\rm secular}^2 a \\ a &= \left(\frac{e^2}{m\omega_{\rm secular}^2}\right)^{1/3}. \end{aligned} \tag{4.24}$$

With $\omega_{\rm secular} = 70 \times 2\pi$ kHz, we obtain $a \simeq 16$ μm. Since this is the estimation from only two ions, the exact value of a must be less than 16 μm. The condition of the formation of the crystal is that the temperature of the ion cloud, T, must be less than 6 mK. We can see that we can easily reach this temperature since the Doppler limit of the ${}^2S_{1/2} \rightarrow {}^2P_{1/2}$ transition, which is our ion cooling transition, is around 530 μK. This is confirmed by the non-Gaussian profile of the ion could in a well compensated trap shown in Figure 4-6. This image is taken using the secondary CCD camera where the y-axis is parallel to the trap axis.

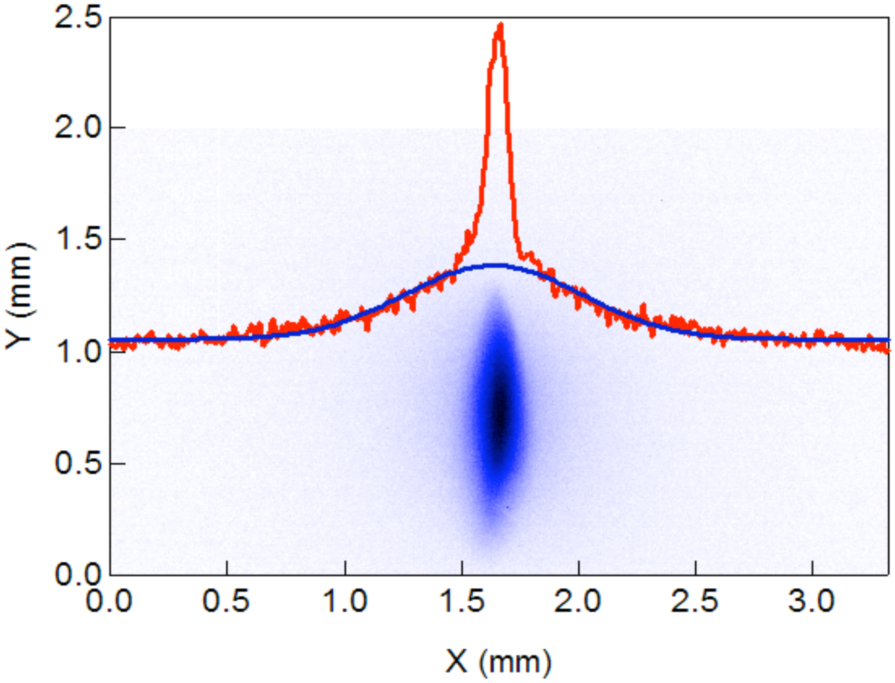

Figure 4-6: Ion crystal taken by the secondary CCD camera along the trap axis. The non-Gaussian profile (red curve) over the background Gaussian fit (blue curve) of the ion cloud indicates that the could is in crystal phase. Image reproduced from [4].

Chapter 5

Setup for the Magneto-Optical Trap and Ion Trap

In this chapter we will discuss the experimental setup for the magneto-optical trap and ion trap. The most important part in the setup is the laser diodes. Luckily all the relevant transitions in our experiment are accessible by laser diodes without resorting to any frequency-doubling non-linear crystal. We will first discuss the setup for the MOT and the ion trap. Then we will show how we can produce ions from the MOT. Finally the image of the trapped ions and the MOT will be shown.

5.1 Laser System

5.1.1 Laser System for Ytterbium Neutral Atoms

In our experiment of atom-ion collisions, the two relevant isotopes of ytterbium are ^{172}Yb and ^{174}Yb. These two isotopes have no hyperfine structure because their nuclei have no spin. The energy level diagram relevant to our experiment is shown in Figure 5-1 The cooling transition is the $^1S_0 \rightarrow ^1 P_1$ transition, giving us the Doppler limit temperature of 690 μK. The light source is a standard near ultra-violet laser diode manufactured by Nichia. The total output power from the diode delivered to the MOT is 10-12 mW divided into three counter-propagating pairs of the MOT.

We use two identical temperature-stabilized laser diodes at 399 nm.[1] Some of the power (around 1.2 mW) of the first laser diode, the so-called master laser, is

---

[1] See Appendix A for temperature stabilization used in our experiment.

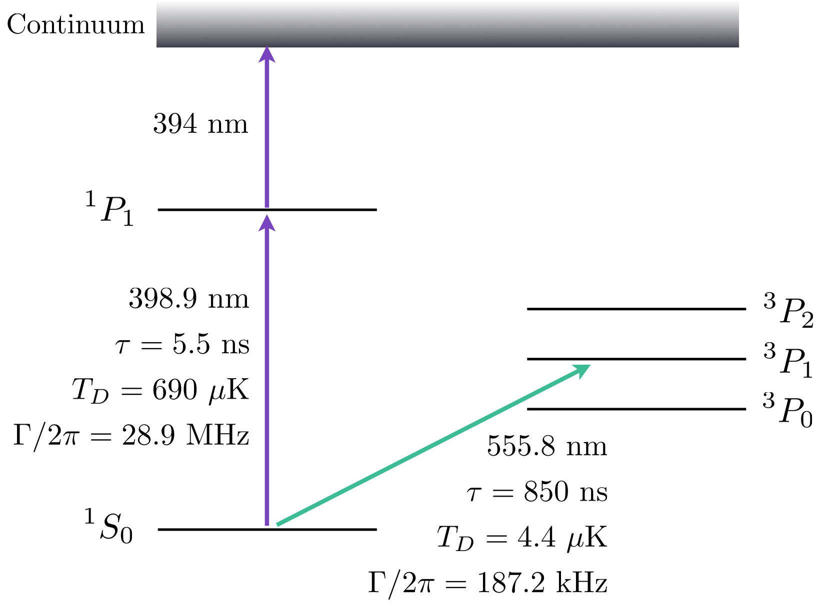

Figure 5-1: Energy level diagram of neutral ^{172}Yb and ^{174}Yb.

injected into the second laser diode, the so-called slave laser diode, to mutually lock the frequency of the two laser diodes. To stabilize the frequency of the master laser diodes, we use a grating to provide a feedback in the Littrow configuration back into the laser. The slave laser diode is only temperature stabilized and has no grating on it. This is sufficient since the injection lock will automatically reduce the line width and stabilize the frequency of the slave laser. To lock the frequency of the master laser diode, we use the Dichroic Atomic Vapor Laser Lock (DAVLL) technique [25].

The DAVLL technique makes use of the Zeeman splittings of the ytterbium atoms in the cathode lamp. The levels with different magnetic quantum numbers will shift in opposite directions. The $^1P_1$ state will split into three sub-levels ($m = -1, 0, 1$). If we excite the atom from $^1S_0$ state using a circularly polarized light, the selection rule requires that the change in magnetic quantum number must conserve the total angular momentum. We use a linear polarized light, which contains both σ^+ and σ^- components, as a probe laser. By scanning the frequency of the probing laser, we can create an error signal by subtracting the absorption curve of one polarization from another polarization curve. The result is the error signal crossing zero at the resonance frequency for $m = 0$. Since we can choose which isotope of ytterbium in the cathode lamp to lock to by simply changing the lock point, we can easily select

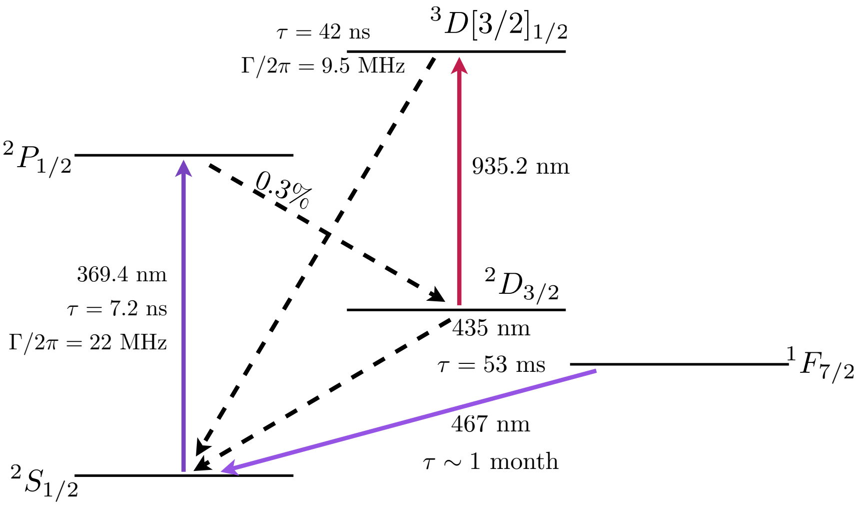

Figure 5-2: Energy level diagram of ^{172}Yb$^+$ and ^{174}Yb$^+$.

which isotope of Yb we want to trap in the MOT. This provides us isotope selectivity which will be useful in the atom-ion collision experiment. The details of the setup of the DAVLL used in our experiment can be found in [3].

5.1.2 Laser System for Ytterbium Ions

The energy diagram for ^{172}Yb$^+$ and ^{174}Yb$^+$ is shown in Figure 5-2. The cooling transition is the $^2S_{1/2} \rightarrow^2 P_{1/2}$ transition. Again, this can be accessed by a single laser diode. The wavelength of the laser diode at room temperature is, however, at 372 nm. We can reach the operating wavelength of 369.4 nm by cooling the diode can down to -45 ^{o}C. This is done by using a two-stage cooling TEC with a water cooling system.

The situation for the ions is a little bit trickier than the neutral Yb case since the $^2P_{1/2}$ state also has a 0.3% chance of falling to $^2D_{3/2}$ state instead of falling directly to $^2S_{1/2}$ state. The lifetime of the $^2D_{3/2}$ state is 53 ms, which is significantly longer than the lifetime of the $^2S_{1/2} \rightarrow^2 P_{1/2}$ transition, which is 7.2 ns. This branching reduces significantly our cooling efficiency. It is then necessary to deplete atomic population in the long-live $^2D_{3/2}$ state by applying a repumper laser at 935.2 nm which will excite

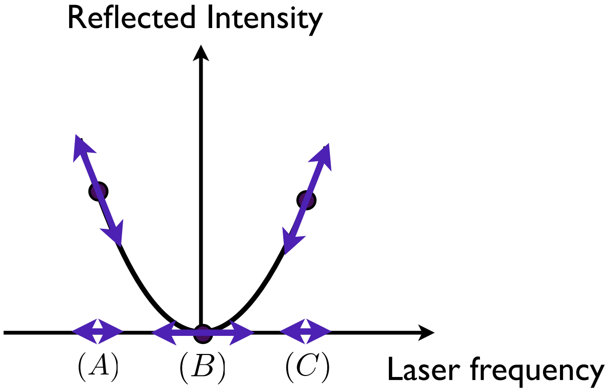

Figure 5-3: Reflected signal from a Fabry-Perot cavity. On resonance (B), the reflected intensity is first-order insensitive to the frequency modulation of the input light. The phase of the intensity modulation compared to the input light will depend on whether the light is red (A) or blue (C) detuned.

the atom from the ${}^2D_{3/2}$ to the ${}^3D[3/2]_{1/2}$ state. The atoms in the ${}^3D[3/2]_{1/2}$ state will rapidly decay back to the ground state with the lifetime of 42 ns and the cooling cycle can proceed as usual.

5.1.3 Pound-Drever-Hall Technique

Since we do not have any atomic reference for the ions, we cannot use the DAVLL technique to lock the ion cooling laser and the repumper laser. We have to use the so-called Pound-Drever-Hall (PD) technique to lock the laser diodes to extenal Fabry-Perot cavities where we can tune the cavity length to tune the locking frequency.

The idea of the PD lock can be illustrated in Figure 5-3. We look at the reflected light from the Fabry-Perot cavity. [2] On resonance, most of the light will be transmitted and the reflected light will have zero intensity. If we shake the frequency of the input light around this point (A), we will not see any change in the intensity to the first-order approximation. If, instead, we are red detuned from the resonance or the point (A) on in the figure, as we shake the frequency from left to right the intensity will change from high to low. Now on the blue detuned side, the intensity will change

---

[2] We can also look at the transmitted signal.

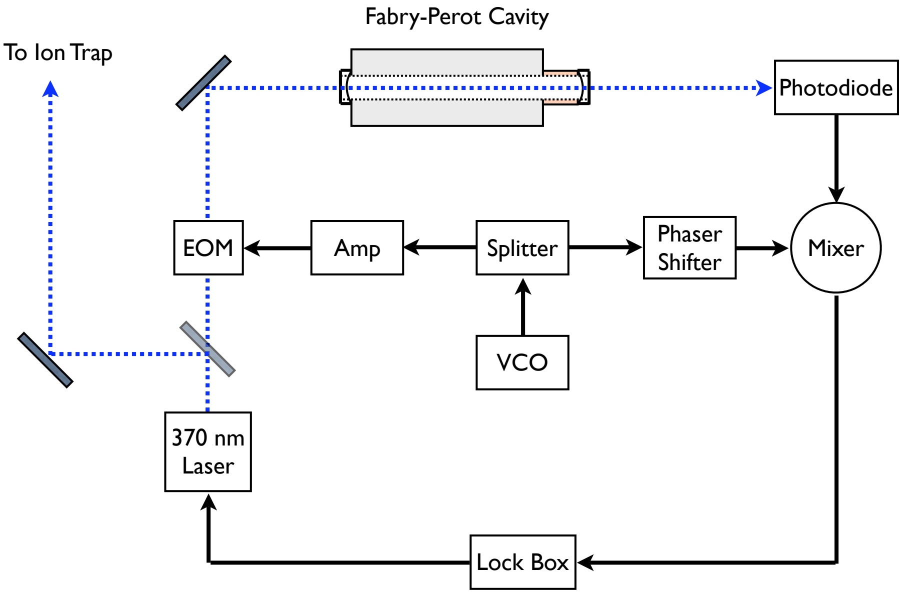

Figure 5-4: Complete Pound-Drever lock diagram. The dotted-line is the optical signal. The black solid line is the electric signal.

from low to high. By looking at the phase of the modulation, we can know which side we are on the resonance curve. This is the error signal which we will feed into the feedback loop to stabilize the frequency around the resonance point. The diagram of the complete Pound-Drever lock is shown in Figure 5-4. Note that in this setup, the transmitted signal is detected by the photodiode instead of the reflected one. The modulating frequency is generated by a voltage-controlled oscillator (VCO) at around 13.5 MHz. Around -3 dBm of this rf signal is fed into the amplifier which will directly modulate the laser light using an electro-optical modulator (EOM). The remaining 7 dBm is used as a local oscillator for a mixer (Minicircuit: TAK-5+). The error signal is extracted from the reflected (or transmitted) intensity by this mixer, and this signal is fed into a lock box which will change the laser frequency accordingly through current modulation. The phase shifter is used to optimize the error signal.

Although every laser diode in the setup is temperature stabilized, according to the fact that the PD lock is sensitive to the Fabry-Perot cavity length, it is also crucial to temperature stabilize the cavity if we want to achieve the highest frequency stability possible. The Fabry-Perot cavity used in our experiment is shown in Figure 5-5. The

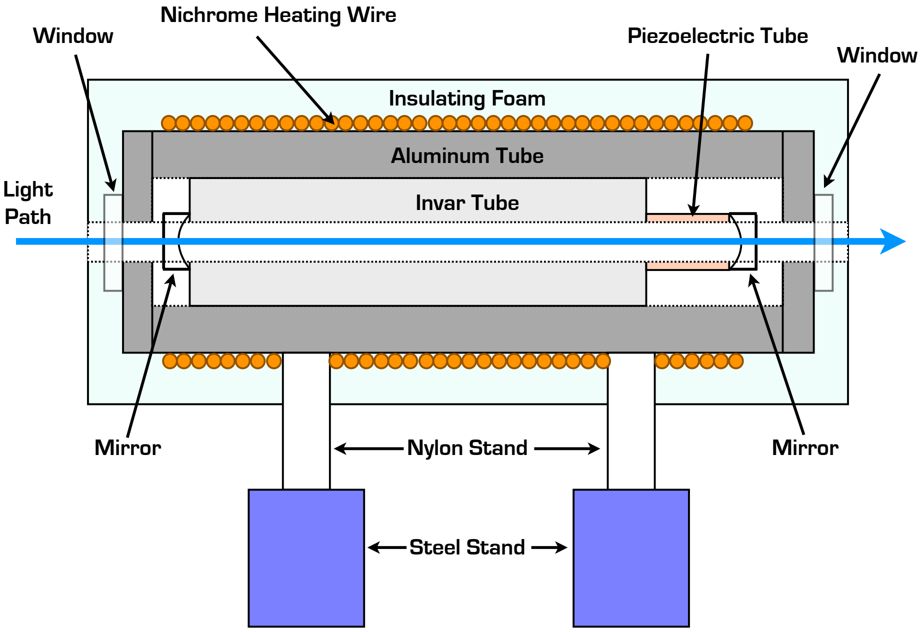

Figure 5-5: Fabry-Perot cavity with temperature stabilization.

core cavity is an Invar® (low thermal expansion coefficient nickel steel alloy) tube with mirrors glued to both ends. The piezoelectric tube is used to adjust the cavity length. By applying 0-150V to the piezoelectric tube, we can adjust the length to at least twice the free spectral range. The Invar® tube is then inserted into an aluminum tube to prevent air current. We wrap the aluminum tube by a nichrome wire to give us better temperature stabilization. This heating wire is analogous to the TEC used in the laser diode system. The whole cavity is then wrapped by an insulating foam tube to minimize heat loss into the environment. The nylon stands are attached to the tube to prevent any heat flow to the steel optical bench. The simplified laser setup is shown in Figure 5-6. Every laser diode has an isolator to filter unwanted reflected light. The ion laser is fiber-coupled through single mode fiber-optics to free-up the space on the optics bench.

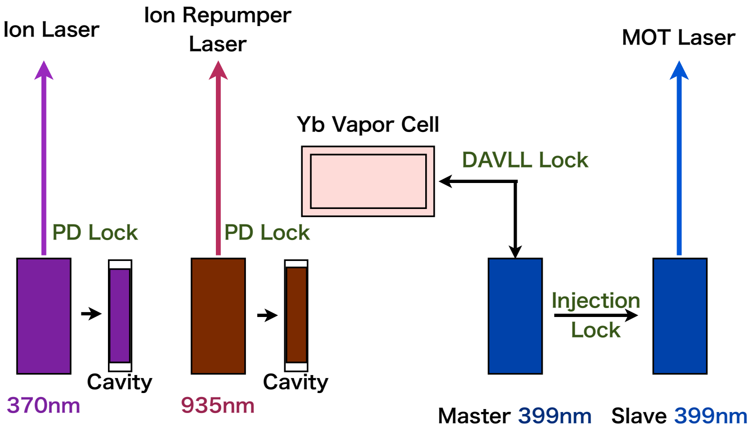

Figure 5-6: Simplified laser system for ytterbium MOT and ion trap. Image reproduced from [4].

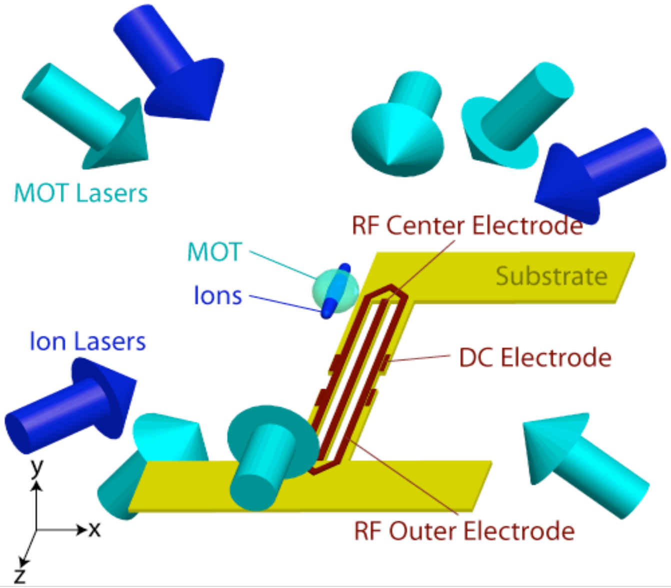

Figure 5-7: MOT-ion trap hybrid setup. Note that the repumper laser is not shown in this figure. Image courtesy of Marko Cetina.

5.2 Magneto-Optical Trap and Ion Trap Hybrid

The planar trap is put in the vacuum chamber. We use a mechanical pump to perform an initial pumping step, then we turn on the ion pump to keep the pressure in side the chamber to around 10^{-7} mTorr. The magnetic field produced by the ion pump around the trapping point is less than 1 G so it is not necessary to shield the pump with any mu-metal. The Ti-sulimation pump also aids us in removing any residues in the chamber.

To produce ions, first we load ytterbium atoms from an oven into the isotope selective MOT. We then photoionize atoms in the MOT optically. The ions produced will not see the MOT since the resonance wavelength is no longer at 399 nm. They will, however, feel the trapping potential generated by the Paul trap. Since the atoms in the MOT are cooled down to the Doppler limit temperature (690 μK), the ions produced will be cold enough to stay in the ion trap. The MOT-ion trap hybrid is shown in Figure 5-7. Due to the open geometry of the Paul trap, it is not difficult to align the laser beams such that we have the ions and the atoms at the same spatial region. However, in the ions loading scheme, it is not absolutely crucial to perfectly overlap the MOT and the ions, since the MOT cloud is usually sufficiently large.

5.2.1 Ion Production

Luckily, the wavelength of the light needed to photoionize ytterbium atom is 394 nm. We can simply use the ion cooling laser as a photoionizing beam, or we can use a separated broadband UVLED to photoionize the atoms. To detect the ions produced, we use a Burle 5901 Magnum Channeltron Electron Multiplier$^{\text{TM}}$(CEM). With both the MOT and the UVLED on, the Channeltron can detect ions up to 227 kHz. With the MOT on but not the UVLED, the ions count is 4.9 kHz [3, 20]. Clearly, the presence of the UVLED highly enhance the ions production rate. The non-zero count rate when the UVLED is off is due to ion production from background atom-atom collisions and other sources. Figure 5-8 shows the ion loading rate from different ionization mechanism. For convenience in our experiment, we use only the 370 nm ion cooling laser to photoionize the atoms.

With ions in the chamber, we can simultaneously trap atoms and ions in the same spatial region. We use a CCD camera with different filters to take the fluorescence pictures of the ions and atoms. The false color image of the ions and the atoms is shown in Figure 5-9. We can move the atomic cloud around by adjusting the bias coil

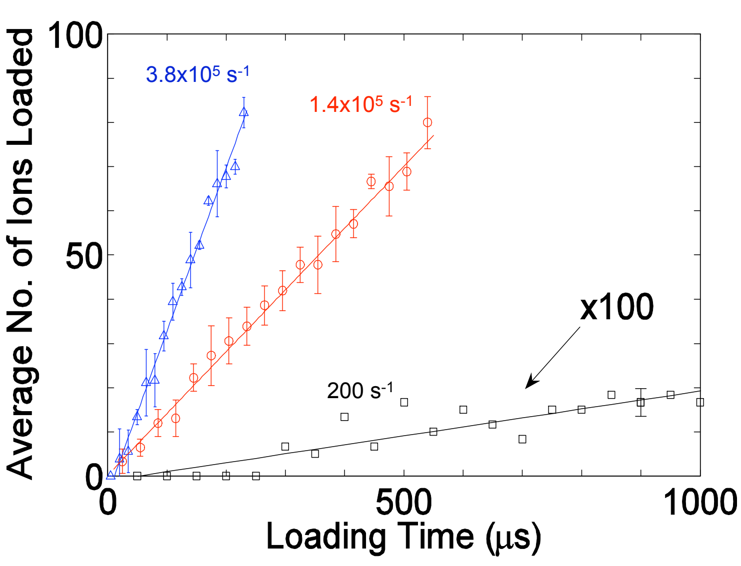

Figure 5-8: Ion loading rate with different photoionization sources. The highest loading rate is when both UVLED and 370 nm ion cooling laser are used (blue triangle). With only UVLED alone, the loading rate is slightly lower (red circle). The loading rate is extremely low from an atomic beam along (black squares). Image reproduced from [2].

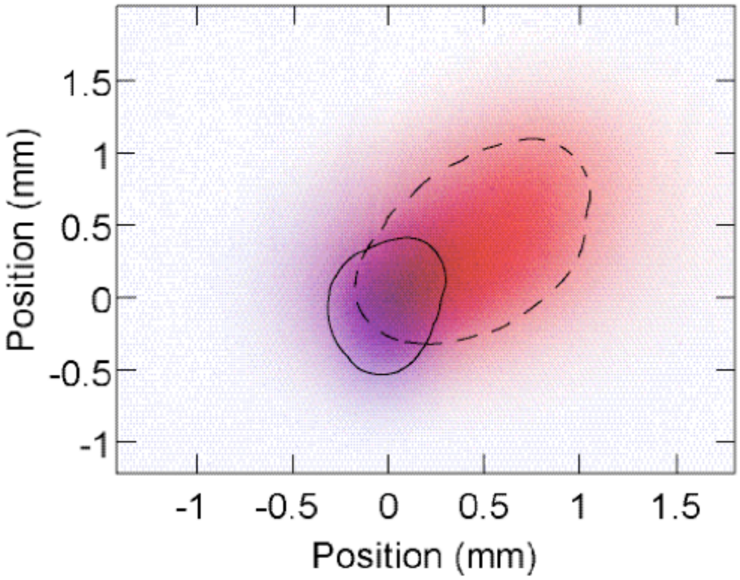

Figure 5-9: MOT-ion overlap taken by the primary CCD camera. The red cloud is the atomic cloud. The violet cloud is the ion cloud. Image reproduced from [2]

to offset the position of the minimum of the magnetic field produced together from the anti-Helmholtz coil. To move the position of the ion around, we can change the voltage applied to the electrodes around the main electrodes as shown in the previous chapter.

Chapter 6

Measurements of Ytterbium Atom-Ion Collisions

Having discussed all the required components for the atom-ion collision experiment, in this chapter we will discuss the experiment procedure. We first describe how we prepare the MOT and the ions of different species, namely, $^{172}\text{Yb}^+$ ions and ^{174}Yb atoms in the MOT. The lifetime of the ions in the trap, as we saw in Chapter 2, depends on the atomic density seen by the ions. The measured decay constants are used to calculate the charge transfer collisional rate and the atomic polarizability.

6.1 MOT-Ion Preparation

To measure the charge transfer cross section between $^{172}\text{Yb}^+$ and ^{174}Yb, we prepare $^{172}\text{Yb}^+$ ions in the trap and the ^{174}Yb atoms in the MOT. The first step is to lock the MOT laser to the ^{172}Yb line and trap ^{172}Yb in the MOT. We then use the 370 nm laser to ionize ^{172}Yb atoms and produce $^{172}\text{Yb}^+$ ions in the trap. To ensure constant trap exposure to the 370 nm light, we pulse the MOT and ions laser at the period of 20 μs with 70% "on" time and 30% "off" time. This is shown in Figure 6-1 as the "$^{172}\text{Yb}^+$ loading" period. In this period, the ion laser and MOT laser are "in phase," namely they are both on and off at the same time.

To cool the ions without producing any more ions from the MOT, we now operate the out-of-phase MOT laser and the ion laser. The MOT laser is on for 70% and off for 30% of time, while the ion laser is off for 70% and on for 30% of time. Since the ions are confined in the trap, only a 30% cooling duty cycle with 20 μs period is adequate.

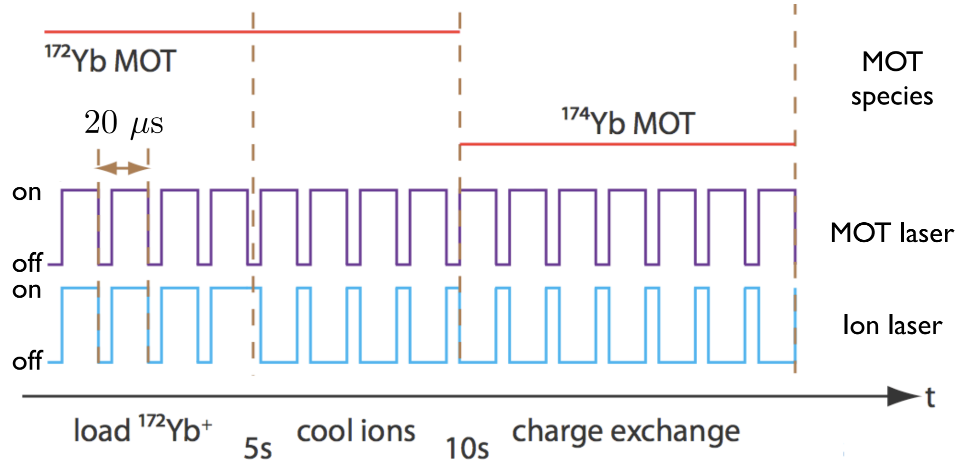

Figure 6-1: Experimental sequence of MOT and ion lasers.

This is called the “cool ions” period. The last step is to switch the MOT laser to the ^{174}Yb line to trap ^{174}Yb in the MOT. The system now consists of ^{174}Yb atoms in the MOT and ^{172}Yb^{+} ions in the trap. During this time the charge transfer takes place, and from this point we can examine the ions lifetime with different atom-ion overlaps.

6.2 Estimation of Atomic Density and Atomic Number

One important parameter that we can measure from the CCD camera is the overlap atomic density between the atoms and ions. In Chapter 2, we state that the average atomic density is given by

$$\langle n_a \rangle = \frac{\int_{-\infty}^{\infty} n_i(\vec{r}) n_a(\vec{r}) dV}{\int_{-\infty}^{\infty} n_i(\vec{r}) dV}. \tag{6.1}$$

We can instead view the whole ion cloud as a single ion with different probability of being at any given point in the cloud. It is natural to write this probability as

$$p_i(\vec{r}) = \frac{1}{N_i} n_i(\vec{r}), \tag{6.2}$$

with

$$\int_{\infty}^{\infty} p_i(\vec{r}) dV = 1, \tag{6.3}$$

where N_i is the total number of ions. The atomic density then can be written as

$$\langle n_a \rangle = \int_{-\infty}^{\infty} p_i(\vec{r}) n_a(\vec{r}) dV. \tag{6.4}$$

Let us look at the Figure 5-9 again. Since our image is a projection onto a plane of the whole ion cloud, we will model the ion density profile to be two-dimensional Gaussian, i.e.,

$$p_i(x, y) = \frac{1}{\sigma_{i,x}\sigma_{i,y}2\pi} e^{-(x-\bar{x}_i)^2/2\sigma_{i,x}} e^{-(y-\bar{y}_i)^2/2\sigma_{i,y}}, \tag{6.5}$$

where $\sigma_{i,x}$ and $\sigma_{i,y}$ are the FWHM of the ion cloud in the x and y direction, respectively, and $\bar{x}_i$ and $\bar{y}_i$ are the position of the ion cloud in the two directions, respectively. For the atomic density, we have

$$n_a(x, y) = \frac{N_a}{\sigma_{a,x}\sigma_{a,y}2\pi} e^{-(x-\bar{x}_a)^2/2\sigma_{a,x}} e^{-(y-\bar{y}_a)^2/2\sigma_{a,y}}, \tag{6.6}$$

where N_a is the total atomic number and other parameters defined analogously to what we have in (6.5). With the area of each pixel of the CCD camera being $\Delta x \Delta y$, we can write (6.4) as

$$\langle n_a \rangle = \frac{\eta}{\Delta x \Delta y} \sum p_i(x, y) n'_a(x, y), \tag{6.7}$$

where η is the correction factor that we use to recover the density in three dimensions and $n'_a(x, y)$ is the actual count of the atomic number in each pixel. For our experiment, the pixel dimensions of the CCD camera are 2 μm × 2 μm. With the optics, this corresponds to the actual spatial dimensions of 8.3 μm × 8.3 μm.

The factor η represents our lack of knowledge of the atomic and ion density profiles in the z direction. We will again assume that the density profile in the z direction is also Gaussian for both atoms and ions. To a very good approximation, the FHWM of the profiles in the z direction is given by

$$\sigma_z = \sqrt{\sigma_x \sigma_y}. \tag{6.8}$$

Combining the contribution from the atomic and ion density, we can write

$$\begin{aligned}\eta &= \frac{1}{\sqrt{(\sigma_{i,z}^2 + \sigma_{a,z}^2)2\pi}}, &(6.9)\\ &= \frac{1}{\sqrt{(\sigma_{i,x}\sigma_{i,y} + \sigma_{a,x}\sigma_{a,y})2\pi}}. &(6.10)\end{aligned}$$

With this, the estimated atomic density for a single ion is given by

$$\langle n_a \rangle = \frac{1}{\Delta x \Delta y \sqrt{(\sigma_{i,x}\sigma_{i,y} + \sigma_{a,x}\sigma_{a,y})2\pi}} \sum p_i(x,y) n_a'(x,y). \tag{6.11}$$

Note that we use $n_a'(x,y)$, the actual count from the CCD camera to calculate $\langle n_a \rangle$. However, in order to obtain $\sigma_{a,x}$ and $\sigma_{a,y}$, we have to fit the profile to the Gaussian function using (6.6).

The estimation of the atomic number is done by comparing the fluorescence signal from a single $^{172}\text{Yb}^+$ ion to the fluorescence signal from ^{174}Yb atoms. We measure that a single $^{172}\text{Yb}^+$ ion in the trap will produce $20 \pm 2 \times 10^3$ counts per second. We then convert back to the case of ^{174}Yb atoms, taking into account the loss in optics, quantum efficiency of the equipments and difference in wavelengths. With these we estimate that a single atom will produce $13 \pm 1 \times 10^3$ counts per second and finally calculate the total atomic number for each measurement.

6.3 Lifetime of the Ions in the Trap

The ion laser, which is locked to be on-resonance with the $^{172}\text{Yb}^+$ ions, is also used as an ion detection beam. The fluorescence from the ions is collected by a photomultiplier. Due to isotope shift, the $^{174}\text{Yb}^+$ produced from charge transfer collisions will not be resonant with the $^{172}\text{Yb}^+$ laser and not be seen. Hence, the fluorescence signal of the $^{172}\text{Yb}^+$ ions will decay according to the expression we derive in Chapter 2, i.e.,

$$N(t) = N(0)e^{-\Gamma t} = N(0)e^{-n_a \sigma_{\text{ch}} v_i t}. \tag{6.12}$$

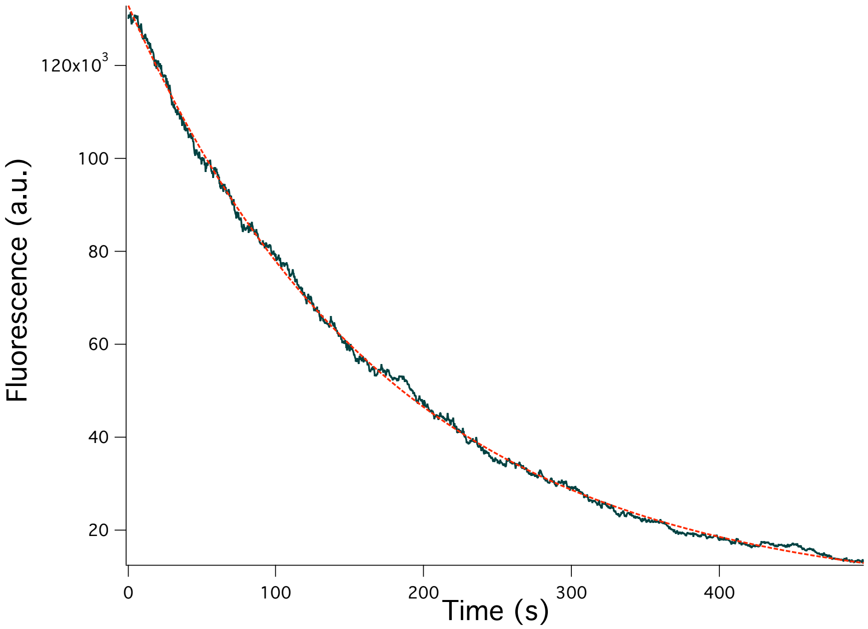

Figure 6-2: ^{172}Yb^{+} ion fluorescence signal at small atom-ion overlap. The population of the ions is well-described by the exponential decay. The lifetime of the ions measured in this case is 176.6±0.4 s.

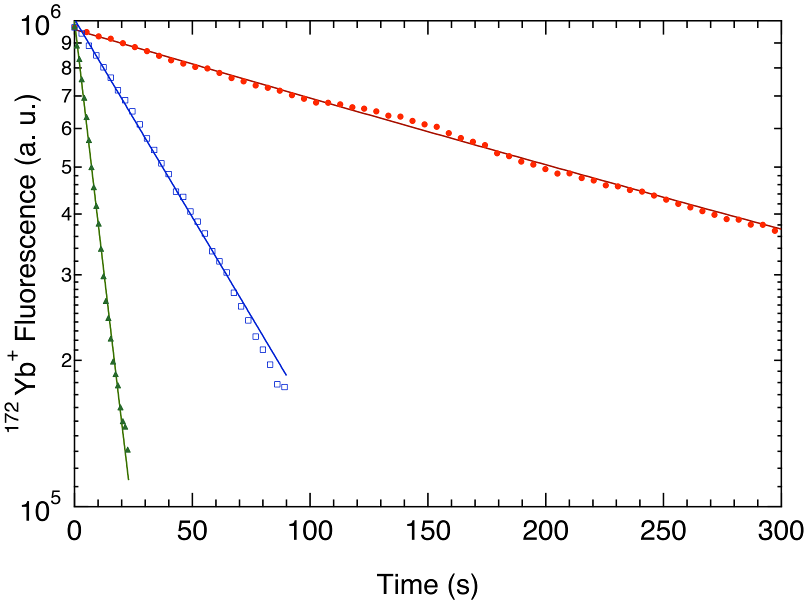

Figure 6-3: ^{172}Yb$^+$ ion fluorescence signal at different atom-ion overlaps. The natural lifetime of the ions (with no MOT) is 288.7±1.6 (red circles). At a moderate overlap, the lifetime of the ions becomes 53.3±0.5 s (blue rectangles). The ions lifetime at the maximum overlap is 10.4±0.2 s (green triangles). Image reproduced from [4].

Figure 6-2 shows the typical fluorescence signal from the 370 nm ion laser. We can see that it is well-described by an exponential decay function. In this case, the overlaps density between the atoms and ions is low, and the life time of the ions is around 176.6±0.4 s. With the absence of the MOT, the ions lifetime can be as long as 300 s.

While keeping the same ion trap configuration, we vary the overlap between the atoms and ions by moving the MOT around using a magnetic field produced by a set of biased coils. We then observe different decay time constants as shown in Figure 6-3. The red circles show the natural lifetime of the ions taken where there is no MOT present, amounting to measured lifetime of 288.7±1.6 s. The blue rectangles show the lifetime of the ions at a moderate overlap, measured as 53.3±0.5 s. When we move the MOT and ions to have maximum overlap, the lifetime drops to 10.4±0.2 s. It is clear that at any overlap, the ^{172}Yb$^+$ ion fluorescence signal is exponential. Different decay constants correspond to different n_a (or, rather, $\langle n_a \rangle$) in (6.12).

Table 6.1: Measured Doppler broadening width, effective temperature and collisional energy.

Doppler Shift (MHz)	E_c (a.u.)
19	8.12×10^{-7}
29	1.89×10^{-6}
37	3.07×10^{-6}
58	7.56×10^{-6}
265	1.58×10^{-4}

6.4 Measurement of Collisional Energy

The decay rate constant is, again, given by

$$\Gamma = \langle n_a \rangle \, \sigma_{\mathrm{ch}} v_i. \tag{6.13}$$

With $v_i = \sqrt{2E_c/\mu}$, we can write

$$\sigma_{\mathrm{ch}} = \frac{\Gamma}{\langle n_a \rangle} \sqrt{\frac{\mu}{2E_c}}. \tag{6.14}$$

From the previous section, we know $\langle n_a \rangle$ from the picture taken from the primary CCD camera. In order to calculate the charge transfer cross section, σ_{ch}, we have to measure the collisional energy, E_c, which we extract from the Doppler fluorescence profiles of the ions. The 369 nm ion laser is locked to the cavity using the Pound-Drever-Hall lock as we discussed in Chapter 5. We can slowly scan the length of the Fabry-Perot cavity, resulting in scanning the frequency of the ion laser. We can look at the fluorescence profiles of the ions across a wide range of the laser frequency.

Since the motion of the ions is driven by the rf field, the motion is not thermal and we cannot use the regular Doppler broadening to measure the temperature of the ions directly. The full analysis of the driven motion with the line width of the cooling transition and laser all taken into account is not analytic. We can, however, estimate the velocity of the ions by simply taking the FWHM (or HWHM) point of the Doppler

Table 6.2: Measured Atomic Polarizability for Ytterbium.

α (SI)	α (a.u.)	E_c (a.u.)	E_c (eV)	$\Gamma/\langle n_a\rangle$ (cm^{3}s^{-1})
3.021×10^{-39}	183.4	8.12×10^{-7}	2.2×10^{-5}	6.56×10^{-10}
2.116×10^{-39}	128.5	1.89×10^{-6}	5.1×10^{-5}	5.49×10^{-10}
2.769×10^{-39}	168.1	3.07×10^{-6}	8.4×10^{-5}	6.28×10^{-10}
3.208×10^{-39}	194.8	7.56×10^{-6}	2.1×10^{-4}	6.76×10^{-10}
8.649×10^{-39}	525.2	1.58×10^{-4}	4.3×10^{-3}	1.11×10^{-9}

curves, shown in Figure 6-4, to be the point where the ions have maximum velocity. The doppler shift is given by

$$f = f_0\left(1+\frac{v}{c}\right), \tag{6.15}$$

where f is the frequency of the photon seen by the ion in its rest frame, f_0 is the proper frequency ($f_0 = 8.12\times10^{14}$ Hz), v is the ion velocity in the lab frame and c is the speed of light. We can then write the relative velocity of the ion-atom system to be

$$v_i = c\frac{f-f_0}{f_0} = c\frac{\Delta f}{f_0}, \tag{6.16}$$

since the atoms are cold enough to be treated as being at rest. The collisional energy is then simply

$$E_c = \frac{1}{2}\mu v_i^2 = \frac{1}{2}\mu c^2\left(\frac{\Delta f}{f_0}\right)^2. \tag{6.17}$$

The measured Doppler shifts and equivalent collisional energies are given in Table 6.1. Note that the natural line width of the cooling transition is 22 MHz (or 11 MHz for HWHM), and we have to subtract this line width from the measured Doppler shift to get the actual velocity of the ions.

6.5 Ytterbium Atomic Polarizability

In the Langevin regime, the charge transfer cross section is given by,

$$\sigma_{\text{ch}} = \frac{1}{2}\pi\sqrt{\frac{2\alpha}{E_c}}. \tag{6.18}$$

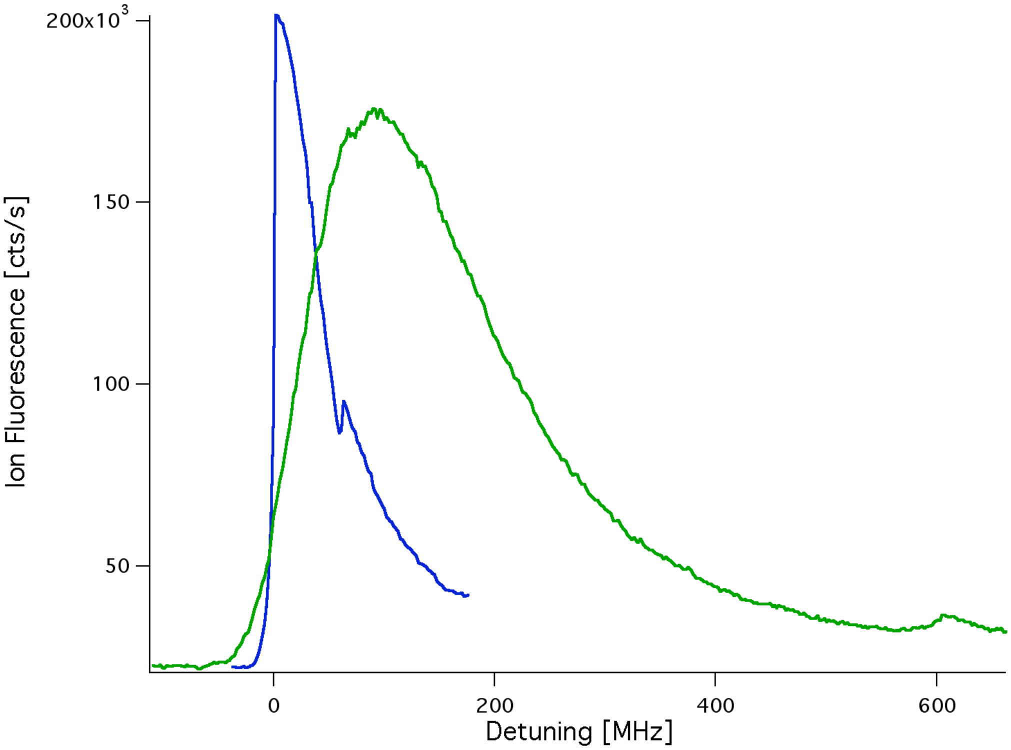

Figure 6-4: ^{172}Yb^{+} Doppler fluorescence profiles measured against the detuning from the center frequency. The Doppler shifts are 69 MHz and 276 MHz for the blue and green curves, respectively. We have to subtract the natural line width of the transition from the measured Doppler shifts. The results are the first two entries in Table 6.1.

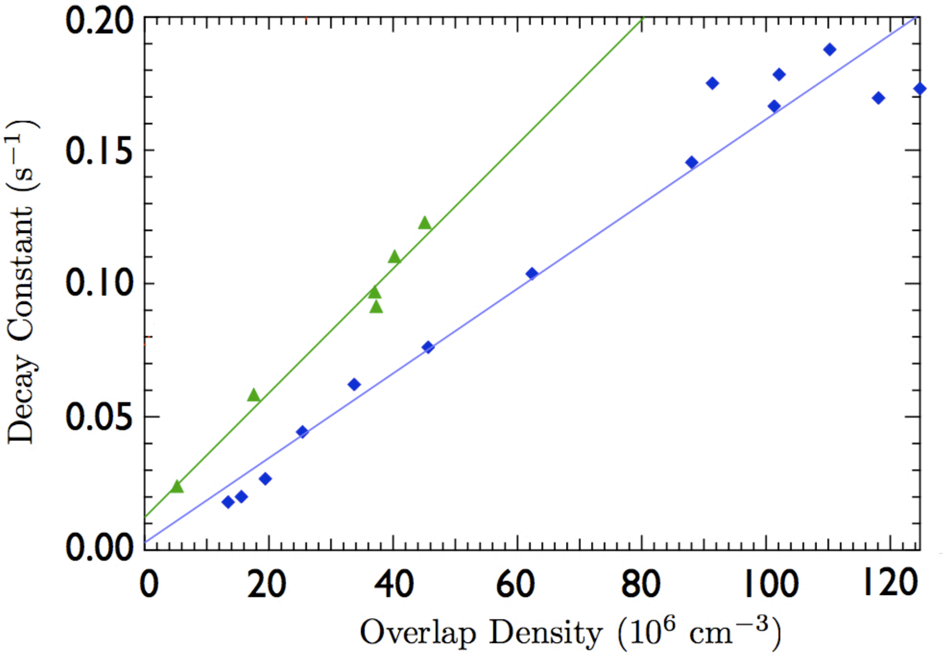

Figure 6-5: Plot of decay rate constant, Γ, against the overlap density, $\langle n_a \rangle$. The green triangle curve is taken at the Doppler HWHM of 269 MHz. The blue rectangle curve is taken at the Doppler HWHM of 69 MHz. The measured values of $\Gamma / \langle n_a \rangle$ are 1.11×10^{-9} cm^{3}s^{-1} and 6.76×10^{-10} cm^{3}s^{-1}, respectively. Image reproduced from [4].

We now can write the polarizability to be

$$\alpha = \frac{\mu}{\pi^2}\left(\frac{\Gamma}{\langle n_a \rangle}\right)^2 \text{ (a.u.)} = \frac{16\epsilon_0^2\mu}{e^2}\left(\frac{\Gamma}{\langle n_a \rangle}\right)^2 \text{ (SI)}. \tag{6.19}$$

The value of $\Gamma/\langle n_a \rangle$ is measured from the plot of the decay rate constant against different overlap density at a given collisional energy. The representative curves are given in Figure 6-5. The calculated atomic polarizability at different collisional energy is given in Table 6.2. The last entry in the table is likely to be the regime where the charge transfer cross section is given by $\sigma_{\text{ch}} = (a \ln E_c + b)^2$ so we can disregard that point for the calculation of the atomic polarizability of ytterbium. The average measured atomic polarizability is

$$\alpha_{\text{measured}} = 169 \pm 14 \pm 85 = 169 \pm 99 \text{ (a.u.)}. \tag{6.20}$$

Note that the first part of the uncertainty comes from statistics of the measurements. The second part comes from the uncertainty in atomic density estimation. Normally, it is difficult to measure the atomic density to have an uncertainty of less than 50%, and this contributes most to the total uncertainty of the measured atomic polarizability. The theoretical value calculated by Zhang and Dalgarno [1] of α is given to be 143 a.u., which is within our measured value of the atomic polarizability. We also confirm that, by looking at Table 6.2, the charge transfer rate is indeed independent of the collisional energy in the Langevin regime.

Chapter 7

Conclusion and Outlook

Using the open geometry of the surface-electrode trap, we can overlap the trapped $^{172}\mathrm{Yb}^+$ ions with the $^{174}\mathrm{Yb}$ atoms in the magneto-optical trap (MOT). The charge transfer collisions between the ions and atoms give rise to the loss of $^{172}\mathrm{Yb}^+$ ions in the trap, resulting in the decay of the fluorescence signal from the ions. The decay rate is directly related to the atomic polarizability of ytterbium, especially in the Langevin regime where the charge transfer cross section is independent of the collisional energy. We can produce ions at collisional energy as low as 2.2×10^{-5} eV, ensuring that we are indeed in the Langevin regime. This is also supported by the fact that the ratio of the decay constant over the atomic density is constant in the collisional energy range from 2.1×10^{-4} eV down to 2.2×10^{-5} eV, suggesting that the charge transfer rate in this regime is independent of the collisional energy. The measured atomic polarizability of ytterbium is 169 ± 99 a.u. This is in agreement with the theoretically calculated value of 143 a.u. by Zhang and Dalgarno [1].

The large uncertainty in our measurements is due to the estimation of atomic density and total atomic number. Because it is difficult to directly measure the number of atoms in the MOT, the values that we used in our estimation are derived from the picture taken from the CCD camera, which is a projection of the total atomic number on a plane. We have to guess the atomic density profiles in the third direction, and this also contributes to the overall uncertainty of the experiment. Future improvement in the estimation will certainly increase our measured atomic polarizability precision.

Our system provides a robust way of observing the interaction between atoms and ions at low temperature. It is, however, even more interesting to have a system with a few ion numbers or even a single ion, which is important in modern quantum

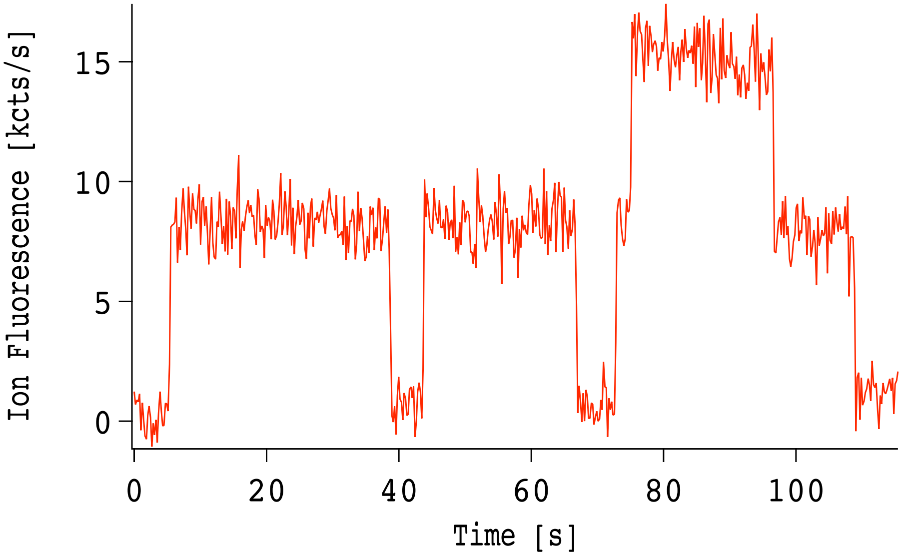

Figure 7-1: Ion fluorescence signal with small number of ions. The characteristic step function of the trace is a clear indication that a single ion is being added or subtracted at time.

computing experiments. The recent measurement also demonstrates the jump of the fluorescence signal, as in Figure 7-1, from adding or subtracting a single ion to or from the ion crystal. With small number of ions, we will be able to see the "turning-off" effect with the collisional energy is less than the ionization energy of the atoms and the charge transfer collisions are prohibited. The lifetime measurement for a single ion can also be done easily once we have tuned our system to have a highly repeatable way of trapping a single ion. Hopefully, our experiment will open new ways to study the system consisting of atoms and ions at very low temperature.

Appendix A

Temperature Stabilization of a Laser Diode

A.1 Basic Theory and Model

A piece of metal will shrink or expand due to its finite thermal expansion coefficient. This change in length also results in frequency changing of a laser diode. If the temperature of a laser diode drifts then the frequency will drift too. To insure that we have highest frequency stability of a laser diode, one need to control and stabilize the laser diode can temperature to the best that one can.

Consider a piece of metal with total heat capacity of C. Due to its interaction with environment, we can write the following equation:

$$C\frac{dT}{dt} = Q, \tag{A.1}$$

where T is the temperature of the system, t is time and Q is the heat transfer into or from the system. According to Newton's law of cooling, Q is generally proportional to the difference between the temperature of the system and room temperature. Basically we can write

$$Q = -K(T - T_e) \tag{A.2}$$

where K is the constant of proportionality and T_e is the room temperature. The minus sign indicates that if the temperature of the system is higher than that of the environment, then heat flows out into environment. Now the basic heat equation is

$$C\frac{dT}{dt} = -K(T - T_e). \tag{A.3}$$

Now we apply a "pump" such that it constantly takes away thermal energy from the system. Normally the pump will work by putting the system in contact with a cold plate. Again, we can apply Newton's law of cooling and state that, by putting a cold plate of temperature T_o, the heat equation now becomes

$$C\frac{dT}{dt} = -K(T - T_e) - \gamma(T - T_o), \tag{A.4}$$

where γ is another constant of proportionality. We can simplify the equation further:

$$\begin{aligned} C\frac{dT}{dt} &= -KT + KT_e - \gamma T + \gamma T_o \qquad (A.5) \\ &= -(K+\gamma)(T - T'_o), \qquad (A.6) \end{aligned}$$

where

$$T'_o = \frac{KT_e + \gamma T_o}{K+\gamma}. \tag{A.7}$$

Notice now that after we solve the differential equation for $T(t)$, we will obtain a exponential decay behavior and eventually the temperature of the system will approach $T(t = \infty) = T'_o$. Note that ideally we want to have a control over the point where the temperature of the system will converge to. T_o depends on both the plate temperature and room temperature which prevents us from putting the set point (or the temperature where the system will converge to) at any temperature we need. Also, the exponential behavior requires long time to reach equilibrium.

We now include the so-called integral gain to the system. The heat equation now becomes

$$C\frac{dT}{dt} = -(K+\gamma)(T - T'_o) - \chi\int_0^t (T - T''_o)dt, \tag{A.8}$$

where χ is a constant and T''_o is the temperature set point which we can choose to be at any temperature. By solving explicitly this simple differential equation for $T(t)$, we arrive at the expression

$$T = Ae^{\frac{-(K+\gamma)+\sqrt{(K+\gamma)^2-4\chi C}}{2C}t} + Be^{\frac{-(K+\gamma)-\sqrt{(K+\gamma)^2-4\chi C}}{2C}t} + T''_0, \tag{A.9}$$

where A and B can be determined from the initial conditions. Usually we will set the parameters such that the system is critically damped. Now the solution becomes

$$T = (A' + B't)e^{-\frac{K+\gamma}{2C}t} + T_0''. \tag{A.10}$$

Again, A' and B' can be determined from the initial conditions. Physical reasoning requires that $B' = 0$. Otherwise at $t = \infty$, T is infinite. The expression now becomes

$$T = A'e^{-\frac{K+\gamma}{2C}t} + T_0''. \tag{A.11}$$

At $t = \infty$, $T = T_0''$, which is the set point that we want the temperature of the system to converge to. This set point appears only in the integral term we added, and does not depend on room temperature or any other temperature.

A.2 Temperature Stabilization Using a Microcontroller

The principle of temperature stabilization can be implemented easily using standard op-amps. However, a properly programmed microcontroller can also be used instead. Since the parameters such as γ and χ in the previous section can be changed easily through reprogramming of the software, it is easier to optimize the parameters compared to re-soldering of various capacitors and/or resistors in a normal op-amp circuit.

Let us recall the heat equation once again:

$$C\frac{dT}{dt} = -K(T - T_e) - \gamma(T - T_o) - \chi\int_0^t (T - T_o'')dt. \tag{A.12}$$

We do not have any control over the first term on the RHS, but we can control T_o, γ, T_o'' and χ. By choosing appropriate value for these parameters, the system can be set such that it is critically damped.

The microcontroller used in the experiment is ATMEGA32L manufactured by Atmel. It has a built-in 10-bit A/D converter and we use that as an input port which receives the temperature reading from a reading stage. This reading stage is setup like a bridge of resistors. A thermistor, being one of the resistor in the bridge, is used to sense the temperature of the system. Resistors bridge is setup such that the net output temperature is read as a voltage drop between two nodes of the bridge. By adjusting one of the resistors in the bridge we can get the differential temperature signal, so-called the error signal, from the reading stage. In this case we use AMP01 instrumentation amplifier before the A/D pin of the microcontroller to further amplify the signal. The 16-bit output from the microcontroller is converted using DAC712 D/A converter. The final stage is the thermoelectric cooling plate (TEC) in which we can adjust the heat pumping rate, Q, by changing the current drawn by the TEC.

We can denote the differential temperature from the reading stage to be $T' = T - \eta$, where η is set by adjusting the resistor in the bridge and T is the absolute temperature. Now (A.12) becomes

$$C\frac{d(T'+\eta)}{dt} = -K(T'+\eta) - \gamma(T'+\eta-T_o) - \chi\int_0^t (T'+\eta-T_o'')dt. \tag{A.13}$$

We know that eventually the temperature of the system will reach a value such that the last term is zero. We can simply set $T_o'' = \eta$ and the final temperature will be $T' = 0$ or $T = \eta$. Since we can set η at any point we want, we can set the set point to be at any temperature by adjusting the potentiometer in the resistor bridge at the reading stage before the input of the microcontroller.

A.3 Application to Fabry-Perot Cavity Temperature Stabilization

In the Pound-Drever-Hall laser locks that we use for the ion laser (370 nm) and the repumper laser (935 nm), we use the same temperature controller as what we use to stabilize the laser diodes to control the temperature of the cavities. Now instead of using TECs to cool down the cavity, we replace them by a nichrome wire to heat up and stabilize the temperature. The main component of the circuit is the same except for the parameters that we can choose and adjust in the software.

One big advantage of using a microcontroller is that we can have more than one different heating-cooling modes, which will be very useful in temperature stabilizing the cavity because a nichrome wire can only heat but not cool. It is more efficient to initially heat up the cavity constantly until the temperature is at the vicinity of the set point temperature. Then we switch from constant heating mode to the normal stabilizing mode. This can be done easily by connecting an external switch to one

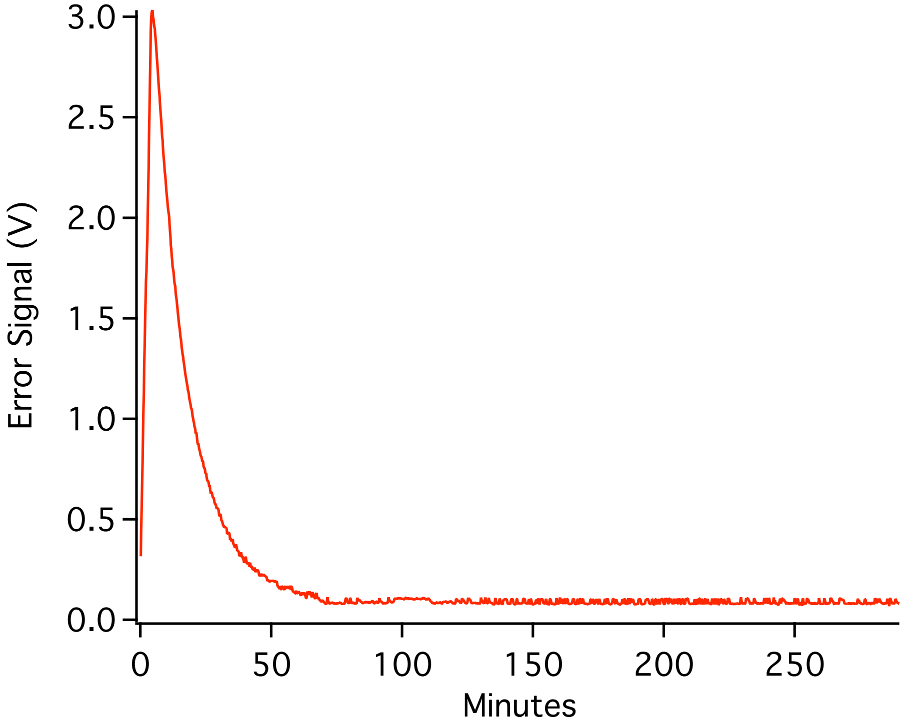

Figure A-1: Error signal or temperature of the cavity measured overnight.

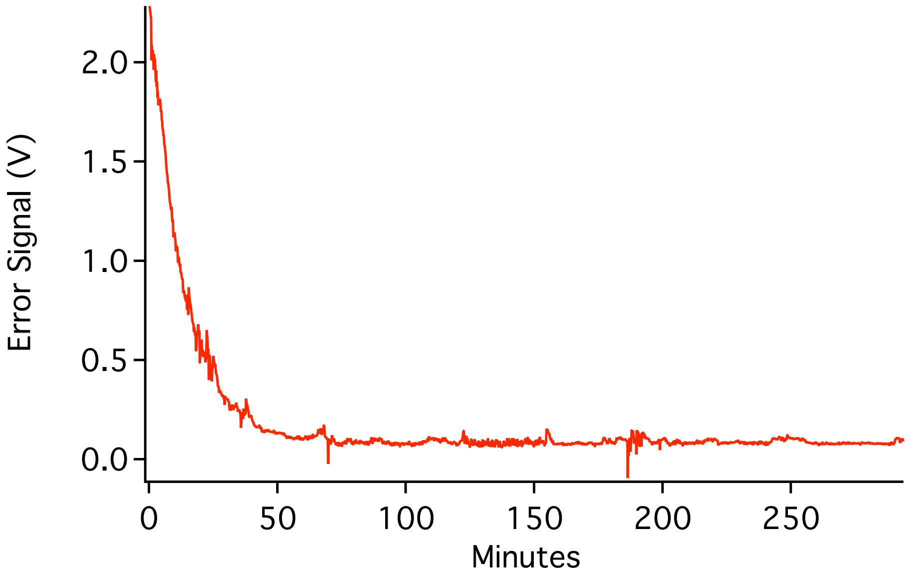

Figure A-2: Error signal or temperature of the cavity measured during the day.

of the unused pins of the microcontroller, and we decide which mode the software will be by looking at the state of that pin. We can also control the working mode of the microcontroller through the RS232 port which can also be easily implemented in both software and hardware.

Figure A-1 and A-2 show the error signal that we monitor for about 5 hours at different time of the day. Both systems receive a short impulse at the beginning so that the exponential decay response is shown in both figures. Figure A-1 is taken overnight, and we can see that the error signal is relatively clean compared to Figure A-2, which is taken during working hours in the laboratory. The non-zero offset of the error signal is due to a small offset of the reading stage and the A/D of the microcontroller. We can adjust this by tweaking the offset parameter in the software but practically there is no difference since the absolute temperature of the set point is not crucial to our experiment as long as the temperature fluctuation is sufficiently small.

A.4 Microcontroller Code in C Programming Language

This section show the actual code in C programming language that we use to program the microcontroller. The parameters in the code or the gain settings are optimized for the Fabry-Perot cavity which uses a long nichrome wire as a heater.

```
#include <mega32.h>  \\Header file for ATMEGA32

const int MAX_INT      = 32767;
const int MIN_INT      = -32768;

#define PROP_GAIN      75   \\Adjust parameters here
#define FIXED_RESULT   9116

#define MULTIPLY_WO_OVERFLOW(c,a,b) {
int t1, t2;
if( (a)>=0 ) t1 =  (a);
else         t1 = -(a);
if( (b)>=0 ) t2 = (b);
```

```
else          t2 = -(b);
if(t1 < MAX_INT/t2)
        (c) = (a) * (b);
else if( ( (a)>=0 && (b)>=0 ) || ( (a)<=0 && (b)<=0 ) )
        (c) = MAX_INT;
else    (c) = MIN_INT;}

#define ADD_WO_OVERFLOW(c,a,b) {
if( (a) >= 0 ) {
        if( (b) <= MAX_INT-(a) )
                (c) = (a) + (b);
        else (c) = MAX_INT;}
else if( (a) > MIN_INT ) {
        if ( (b) >= MIN_INT - a )
                (c) = (a) + (b);
        else (c) = MIN_INT;}
else {
        if( b < 0 )
                (c) = MIN_INT;
        else
        (c) = (a) + (b);} };

int errSignal    = 0;
int integrator   = 0;
int proportional = 0;
unsigned int timecount = 0;

interrupt [TIM0_OVF] void timer0_ovf_isr(void)
{
        int localErrSignal;
        int localIntegrator;
        TCNT0 = 0;            // set the initial counter to 0
        if(++timecount==175)
        {
                timecount = 0;
```

```
                localErrSignal = errSignal;
                localIntegrator = integrator;

ADD_WO_OVERFLOW(localIntegrator,localIntegrator,-localErrSignal);
                integrator = localIntegrator;
        }
}

const int ADCOFFSET  = 8;//this is what DAC outputs at errSignal = 0
const int DACOFFSRET = 0;//this is what ADC outputs with input =0

interrupt [ADC_INT] void adc_isr(void) //ADC ISR
{
        unsigned int adc_data;     // variable for ADC result
        int tmp;       // temporary variable for writing into globals
        unsigned char output;
        int result = 0;
        unsigned char z;
        unsigned char i;
        adc_data = ADCW;        // read all 10 bits
        tmp = (511 - (int)adc_data);// invert the input
        tmp = tmp - ADCOFFSET;
        errSignal = tmp; // the error signal is now 11 bits deep
        MULTIPLY_WO_OVERFLOW(proportional,-errSignal,PROP_GAIN);

        // Constant heating mode.
        if(PINA & 0x08) {
                result     = FIXED_RESULT;
                ADD_WO_OVERFLOW(integrator,result,-proportional);
        }
        else {
                ADD_WO_OVERFLOW(result,integrator,proportional);
        }

        if(result < 0) result = 0;
```

```
        PORTC = ((char*)(&result))[1];// Output pins configuration
        PORTD = ((char*)(&result))[0] & (0xFF-3);
        PORTB = ((char*)(&result))[0] & 3;

        ADCSRA = ADCSRA | 0x40; // start next ADC conversion
}
void main(void)
{
        DDRC = 0xFF;// direction ctrl for port C; port C as output
        DDRA = 0x00;// direction ctrl for port A; port A as input
        TCCR0=0x05;// normal timer/counter opertation
                           // clock =  system CLCK / 1024
        TCNT0=0x00;// Set the initial value of the counter to 0
        TIMSK=0x01;// Enable timer/counter overflow interrupt
        ADMUX = 0b11000000; // Internal 2.56 V-ref, input = pin ADC0
                                // Single ended input
        ADCSRA = 0xCE;
        #asm("sei")  // global interrupt enabled
        while (1)
        ;
}
```

Appendix B

Measurement of the Finesse of Mirrors

In any experiment involving a Fabry-Perot cavity, it is advantageous to have a direct way to measure the finesse of the cavity. We cannot simply look at the line width of the scanning cavity because if the laser line width is wider than that of the cavity, what we will see is simply the laser line width. The cavity ring-down measurement, which basically look at the loss of the photons stored in the cavity as a function of time, provides us a way to measure the finesse of the cavity independent of the laser line width.

B.1 Finesse of a Cavity

Suppose we have two identical mirrors of reflectivity R placed at distance L apart. The finesse of a cavity is defined as

$$F = \frac{\Delta\nu_{\mathrm{FSR}}}{\delta\nu_c}, \tag{B.1}$$

where

$$\Delta\nu_{\mathrm{FSR}} = \frac{c}{2L} \tag{B.2}$$

is the free spectral range, and $\delta\nu_c$ is the cavity line width. The cavity ring-down time is simply given by

$$\tau = \frac{1}{2\pi\delta\nu_c}. \tag{B.3}$$

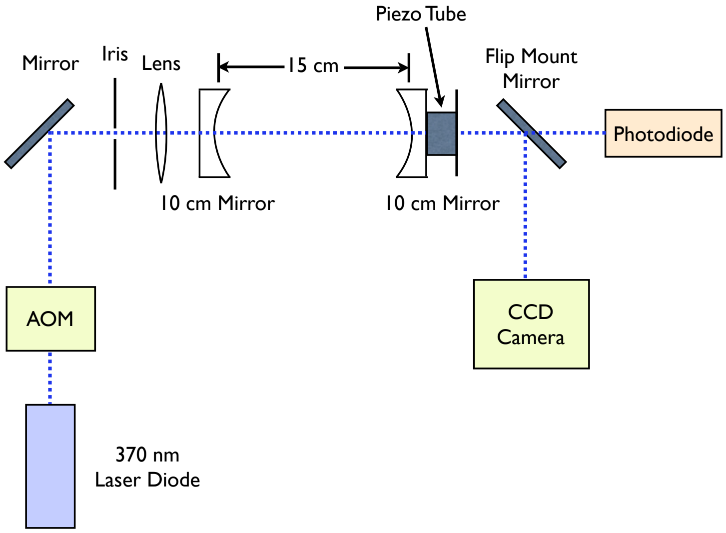

Figure B-1: Setup of the cavity ring-down measurement.

We can measure the cavity ring-down time and calculate the finesse, which is given by

$$F \simeq \frac{\pi\sqrt{R}}{1-R}. \tag{B.4}$$

B.2 Cavity Ring-Down Measurement

The setup of the experiment is given in Figure B-1. We use a 370 nm laser diode as a source. A fast acousto-optic modulator (AOM) is used to turn off the laser within 200 ns. The cavity consists of a pair of identical mirrors each with curvature of 10.0 cm and the distance between the mirrors is 15.0 cm. A piezo tube is attached to one of the mirror for a cavity scanning. A CCD camera looking at the output of the cavity helps us with the alignment and mode matching since we can see the output mode in real time. The output signal is detected by a fast photodiode with a response time of 200 ns. A flip mount provides us an easy way to switch from looking at a photodiode to a CCD camera.

The experimental procedure is to tune the laser on the cavity resonance. At this

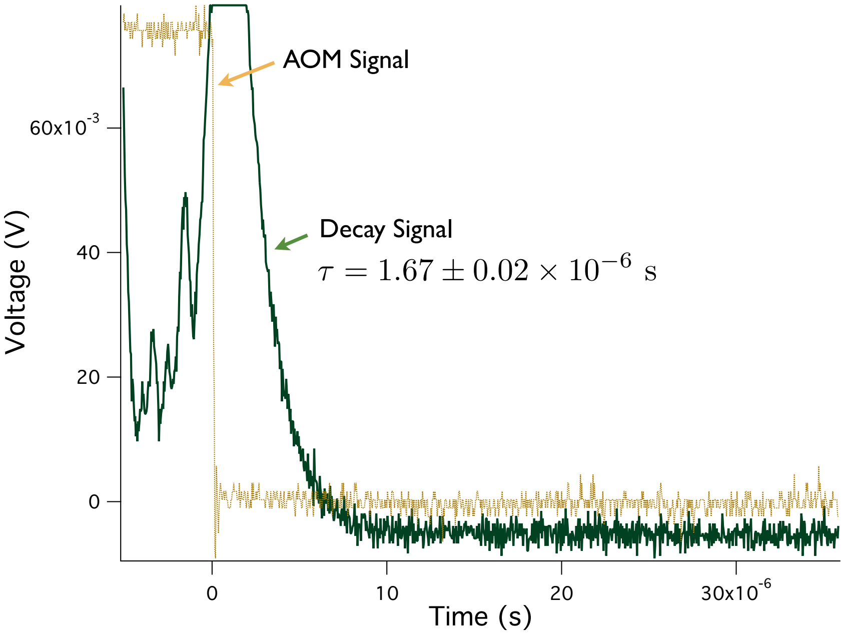

Figure B-2: Representative cavity ring-down decay curve. We fit the curve after the AOM (brown) had cut off the laser light to the exponential decay curve (dark green). The measured decay time from three independent measurements yield $\tau = 1.67 \pm 0.02 \times 10^{-6}$ s .

time the transmission seen by the photodiode will be maximum. Then the AOM will cut off the laser and we can see the decay of the signal in from the photodiode. The representative decay trace that we capture using an oscilloscope is given in Figure B-2.

The measured decay time is $1.67 \pm 0.02 \times 10^{-6}$ s . The calculated finesse from this decay time is

$$\begin{aligned} F &= \Delta\nu_{\text{FSR}} 2\pi\tau \\ &= 10492 \pm 125. \end{aligned} \tag{B.5}$$

We compare this value of finesse to our measured value of the reflectivity of the mirror. The measurement is done by comparing the intensity of the laser light before and after the mirror. The measured value given in Table B.1 is done by measuring the current generated by a photodiode (different from the one used for the cavity ring-down measurement) with and without the mirror in front of the photodiode.

Table B.1: Measured transmission intensity of the 10 cm mirror.

	Voltage (mV)	Resistance (Ω)	Current (mA)
Without Mirror	119.4	5.002×10^3	2.387×10^{-2}
With Mirror	5.6	9.92×10^5	5.645×10^{-6}

The measured fractional transmission is 236×10^{-6}. This gives the calculated finesse to be $f = 13312$. We think that additional loss from the reflecting surface of the mirrors explains why the finesse measured from the ring-down cavity is less than the finesse calculated from only the measured transmission intensity.

Appendix C

Atomic Units

Atomic units normalize to 1 the charge, e, and mass of the electron, m_e, the Planck's constant, $\hbar$, the Bohr radius, a_0, and Hartree energy (twice the magnitude of the ground state hydrogen energy, 2×13.6 eV or $4.359{\times}10^{-18}$ J), H.[1] This is equivalent to setting

$$\begin{aligned} e &= 1 \\ m_e &= 1 \\ a_0 &= \frac{\hbar}{m_e c\alpha} \text{ (SI) } = \frac{1}{c\alpha} = 1 \\ H &= \frac{m_e(e^2/4\pi\epsilon_o)^2}{\hbar} \text{ (SI) } = m_e(\alpha c)^2 \text{ (SI) } = \frac{1}{(4\pi\epsilon_o)^2} = 1 \end{aligned}$$

The fine structure constant, α is $e^2/4\pi\epsilon_0\hbar c = 1/(137.0606...)$. It is dimensionless and the most fundamental constant in atomic physics independent of the units. From the equations above, we can set $c = 1/\alpha$. In SI units, $c = 1/\sqrt{\mu_o\epsilon_o}$. Then,

$$\mu_o = \frac{1}{c^2\epsilon_o} = 4\pi\alpha^2. \tag{C.1}$$

Furthermore, the electromagnetic interaction in atomic physics is usually described in the Gaussian units. The conversion is quite simple. Simply set

$$\vec{B} \text{ (SI) } = \frac{\vec{B}}{c}. \tag{C.2}$$

---

[1] In this chapter, we denote the fine structure constant to be α.

Table C.1: Conversion from SI units to atomic-Gaussian units

Quantity to be replaced	Replace by
e	1
m_e	1
$\hbar$	1
c	$1/\alpha$
$4\pi\epsilon_o$	1
μ_o	$4\pi\alpha^2$
$\vec{B}$	$\vec{B}/c = \alpha\vec{B}$

Note that we have used the atomic unit conversion already. Now we would like to summarize the conversion from SI units to atomic-Gaussian units in Table C.1. Sometimes we would like to keep some quantities around despite the fact that they are, in atomic-Gaussian units, equal to 1. For example, we write the polarization potential to be

$$U(r) = -\frac{\alpha \text{ (polarizability) } e^2}{2r^4},$$

instead of

$$U(r) = -\frac{\alpha \text{ (polarizability)}}{2r^4}$$

just to keep the scaling of e obvious.

Once we have finished switching the quantity given in Table C.1, every quantity must be appropriately expressed in atomic units. Atomic polarizability is a relevant quantity for our discussion of cold collisions. It is helpful to quickly summarize the conversion between atomic units and SI units. Atomic unit for polarizability is expressed in the unit of a_o^3. To convert back to SI units, use the expression

$$\alpha \text{ (polarizability in SI) } = \alpha \text{ (polarizability in a.u.) } \times 1.647 \times 10^{-41} \text{ C}^2\text{m/N}.$$

Appendix D

Evaluation of Hydrogen Molecular Ion Ground State Energy

We now would like to evaluate the energy of the ground state hydrogen molecular ion using the procedure suggested by [12] and [26]. The integral we want to evaluate is

$$E_{g,u}(R) = \frac{\int \Phi^*_{g,u}(\vec{R},\vec{r}) H \Phi_{g,u}(\vec{R},\vec{r}) d\vec{r}}{\int |\Phi_{g,u}(\vec{R},\vec{r})|^2 d\vec{r}} \tag{D.1}$$

where

$$H = -\frac{1}{2}\nabla_r^2 - \frac{1}{r_A} - \frac{1}{r_B} + \frac{1}{R}, \tag{D.2}$$

and

$$\Phi_g(\vec{R},\vec{r}) = \frac{1}{\sqrt{2}}(\psi_{1s}(r_A) + \psi_{1s}(r_B)),$$
$$\Phi_u(\vec{R},\vec{r}) = \frac{1}{\sqrt{2}}(\psi_{1s}(r_A) - \psi_{1s}(r_B)). \tag{D.3}$$

are the “gerade” and “ungerade” states of the molecule. Furthermore, $\vec{r}$, $\vec{R}$, r_A and r_B are coupled through the following expressions:

$$\vec{r} = \frac{1}{2}\vec{R} + \vec{r}_B, \tag{D.4}$$

$$\vec{r} = -\frac{1}{2}\vec{R} + \vec{r}_A. \tag{D.5}$$

D.1 Two-Center Integrals

It is useful to evaluate the integral of the form

$$J = \int \frac{e^{-ar_A}e^{-br_B}}{r_A r_B} d\vec{r}. \tag{D.6}$$

By changing to the new coordinate defined by

$$\epsilon = \frac{1}{R}(r_A + r_B), \tag{D.7}$$

$$\eta = \frac{1}{R}(r_A - r_B), \tag{D.8}$$

the volume element $d\vec{r}$ becomes

$$d\vec{r} = \frac{R^3}{8}(\epsilon^2 - \eta^2) d\eta d\epsilon d\phi. \tag{D.9}$$

Then we have

$$J = \frac{R}{2}\int_1^\infty d\epsilon \int_{-1}^{+1} d\eta \int_0^{2\pi} d\phi e^{-\frac{R}{2}(\epsilon(a+b)+\eta(a-b))}. \tag{D.10}$$

This is just the products of exponential integrals. We get

$$J = \frac{4\pi}{R}\frac{1}{a^2-b^2}(e^{-bR} - e^{-aR}). \tag{D.11}$$

Now if we want to evaluate

$$K = \int \frac{e^{-ar_A}e^{-br_B}}{r_A} d\vec{r}, \tag{D.12}$$

then this is just

$$\begin{aligned} K &= -\frac{d}{db}J \\ &= \frac{4\pi}{R}\left(\frac{R}{a^2-b^2}e^{-bR} + \frac{2b}{(a^2-b^2)^2}(e^{-aR} - e^{-bR})\right). \end{aligned} \tag{D.13}$$

If we want to evaluate

$$L = \int e^{-ar_A}e^{-br_B} d\vec{r}, \tag{D.14}$$

this is just

$$\begin{aligned} L &= -\frac{d}{da}K \\ &= \frac{8\pi}{R(a^2-b^2)^2}\left(R(ae^{-bR}+be^{-aR})+\frac{4ab}{a^2-b^2}(e^{-aR}-e^{-bR})\right). \end{aligned} \tag{D.15}$$

If $a = b = 1$, then we obtain

$$J = 2\pi e^{-R} \tag{D.16}$$

$$K = \pi(1+R)e^{-R} \tag{D.17}$$

$$L = \pi(1+R+\frac{1}{3}R^2)e^{-R}. \tag{D.18}$$

D.2 Hydrogen Molecular Ion Energy

Dropping the subscript $1s$, we first look at the denominator of (D.1):

$$\begin{aligned} D_{g,u} &= \int |\Phi_{g,u}(\vec{R},\vec{r})|^2 d\vec{r} \\ &= \frac{1}{2}\int [|\psi(r_A)|^2+|\psi(r_B)|^2 \pm 2\psi(r_A)\psi(r_B)]d\vec{r}. \end{aligned} \tag{D.19}$$

With normalization of $\psi(r_B)$ and $\psi(r_B)$, we have

$$D_{g,u} = 1 \pm \int \psi(r_A)\psi(r_B)d\vec{r}. \tag{D.20}$$

Recall that $\psi(r_B)$ and $\psi(r_B)$ are the $1s$ wave function of the hydrogen atom. We then have to evaluate

$$\int \psi(r_A)\psi(r_B)d\vec{r} = \frac{1}{\pi}\int e^{-r_A}e^{-r_B}d\vec{r}. \tag{D.21}$$

With (D.18), we have

$$D_{g,u} = 1 \pm (1+R+\frac{1}{3}R^2)e^{-R}. \tag{D.22}$$

We now switch our attention to the numerator of (D.1). We have

$$N_{g,u} = \frac{1}{2}\int \psi(r_A)H\psi(r_A) + \psi(r_B)H\psi(r_B) \pm (\psi(r_A)H\psi(r_B) + \psi(r_B)H\psi(r_A))d\vec{r}. \tag{D.23}$$

By the symmetry of switching r_A and r_B, this is reduced to

$$N_{g,u} = \int \psi(r_A)H\psi(r_A) \pm \psi(r_A)H\psi(r_B)d\vec{r}. \tag{D.24}$$

We first evaluate the first term of (D.24)

$$\int \psi(r_A)H\psi(r_A)d\vec{r} = \int \psi(r_A)\left(-\frac{1}{2}\nabla_r^2 - \frac{1}{r_A} - \frac{1}{r_B} + \frac{1}{R}\right)\psi(r_A)d\vec{r}.$$

Recall that $\psi(r_A)$ is the wave function of the hydrogenic ground state, namely

$$\left(-\frac{1}{2}\nabla^2 - \frac{1}{r_{A,B}} - E_{1s}\right)\psi(r_{A,B}) = 0. \tag{D.25}$$

Then the integral becomes

$$\begin{aligned}\int \psi(r_A)H\psi(r_A)d\vec{r} &= \int \psi(r_A)\left(E_{1s} - \frac{1}{r_B} + \frac{1}{R}\right)\psi(r_A)d\vec{r},\\ &= E_{1s} + \frac{1}{R} - \frac{1}{\pi}\int \frac{e^{-2r_A}}{r_B}d\vec{r}.\end{aligned} \tag{D.26}$$

From (D.12) and (D.13), by setting $a = 0$ and $b = 2$ and switching r_A to r_B, we get

$$\begin{aligned}\int \psi(r_A)H\psi(r_A)d\vec{r} &= E_{1s} + \frac{1}{R} - \frac{4}{R}\left(-\frac{R}{4}e^{-2R} + \frac{1}{4}(1 - e^{-2R})\right)\\ &= E_{1s} + (1 + \frac{1}{R})e^{-2R}.\end{aligned} \tag{D.27}$$

We now evaluate the second term of (D.24)

$$\int \psi(r_A)H\psi(r_B)d\vec{r} = \int \psi(r_A)\left(-\frac{1}{2}\nabla_r^2 - \frac{1}{r_A} - \frac{1}{r_B} + \frac{1}{R}\right)\psi(r_B)d\vec{r}.$$

With (D.25), the integral becomes

$$\begin{aligned}\int \psi(r_A) H \psi(r_B) d\vec{r} &= \int \psi(r_A) \left(E_{1s} - \frac{1}{r_A} + \frac{1}{R} \right) \psi(r_B) d\vec{r}, \\ &= \left(E_{1s} + \frac{1}{R} \right) \int \psi(r_A)\psi(r_B) d\vec{r} - \int \frac{\psi(r_A)\psi(r_B)}{r_A} d\vec{r}, \\ &= \left(E_{1s} + \frac{1}{R} \right) \frac{1}{\pi} \int e^{-r_A} e^{-r_B} d\vec{r} - \frac{1}{\pi} \int \frac{e^{-r_A} e^{-r_B}}{r_A} d\vec{r}. \qquad \text{(D.28)}\end{aligned}$$

With (D.17) and (D.18), we get

$$\int \psi(r_A) H \psi(r_B) d\vec{r} = \left(E_{1s} + \frac{1}{R} \right) (1 + R + \frac{1}{3} R^2) e^{-R} - (1 + R) e^{-R}. \qquad \text{(D.29)}$$

Putting everything together, the ground state of hydrogen molecular ion is

$$E_{g,u}(R) = E_{1s} + \frac{1}{R} \frac{(1 + R) e^{-2R} \pm (1 - \frac{2}{3} R^2) e^{-R}}{1 \pm (1 + R + \frac{1}{3} R^2) e^{-R}}. \qquad \text{(D.30)}$$

Appendix E

Angular Momentum and Spherical Harmonics

The orbital angular momentum operation is defined as

$$\vec{L} = \vec{r} \times \vec{p} \tag{E.1}$$

where $\vec{r}$ is the position operator and $\vec{p}$ is the linear momentum operator. With $\vec{p} = -i\hbar\nabla_r$, it can be easily shown that, in the spherical coordinate system,

$$\vec{L}^2 = L_x^2 + L_y^2 + L_z^2 = -\hbar^2 \left[\frac{1}{\sin\theta} \frac{\partial}{\partial\theta} \left(\sin\theta \frac{\partial}{\partial\theta} \right) + \frac{1}{\sin^2\theta} \frac{\partial^2}{\partial\phi^2} \right] \tag{E.2}$$

where θ and ϕ are defined in a usual way. We can also verify the commutation rules between different components of the angular momentum,

$$[L_i, L_j] = i\epsilon_{ijk} L_k, \tag{E.3}$$

where ϵ_{ijk} is the Levi-Civita tensor.

When specifying the wave function in three dimensions, it is useful to define the spherical harmonics, $Y_{lm}(\theta, \phi)$, by the followings:

$$L^2 Y_{lm}(\theta, \phi) = l(l+1) Y_{lm}(\theta, \phi), \tag{E.4}$$

$$L_z Y_{lm}(\theta, \phi) = m Y_{lm}(\theta, \phi), \tag{E.5}$$

where l is the orbital angular momentum number and m is the magnetic quantum number. The general expression for spherical harmonics is

$$Y_{lm}(\theta, \phi) = \epsilon \sqrt{\frac{(2l+1)}{4\pi} \frac{(l-|m|)!}{(l+|m|)!}} e^{im\phi} P_l^m(\cos\theta), \tag{E.6}$$

where $\epsilon = (-1)^m$ for $m \geq 0$ and $\epsilon = 1$ for $m \leq 0$ and $P_l^m(x)$ is the associated Legendre function, defined by

$$P_l^m(x) = (1-x^2)^{|m|/2} \left(\frac{d}{dx}\right)^{|m|} P_l(x), \tag{E.7}$$

and $P_l(x)$ is the Legendre polynomials defined by

$$xP_l(x) = \frac{1}{2l+1}[(l+1)P_{l+1}(x) + lP_{l-1}(x)] \tag{E.8}$$

with $P_0(x) = 1$ and $P_1(x) = x$.

Bibliography

[1] P. Zhang and A. Dalgarno. J. Phys. Chem. A **111**, 12471-12476, (2007).

[2] M. Cetina, A. Grier, J. Campbell, I. Chuang, and V. Vuletić. Phys. Rev. A **76**, 041401, (2007).

[3] J. A. Campbell. *Surface Trap for Ytterbium Ions.* Master thesis, Massachusetts Institute of Technology, Department of Physics, June 2006.

[4] A. Grier, M. Cetina, F. Orucevic, and V. Vuletic. (to be published).

[5] D. Egorov, T. Lahaye, B. Friedrich W. Schöllkopf, and J. Doyle. Phys. Rev. A **66**, 043401, (2002).

[6] A. Derevianko, R. Côté, A. Dalgarno, and G.-H. Jeung. Phys. Rev. A **64**, 011404, (2001).

[7] H. Goldstein, C. Poole, and J. Safko. *Classical Mechanics.* Addison-Wesley, (2002).

[8] P. Langevin. *Annales de chimie et de physique*, Series 8, **5**, 245-288, (1905).

[9] A. Dalgarno, M.R.C. McDowell, and A. Williams. Philos. Trans. R. Soc. London, Ser. A **250**, 411, (1958).

[10] D. Rapp and W.E. Francis. J. Chem. Phys. **37**, 11, (1962).

[11] N. F. Mott and H. S. W. Massey. *The Theory of Atomic Collisions.* Oxford Science Publication, (1987).

[12] B. H. Brandsden and C. J. Joachain. *Physics of atoms and molecules.* Longman, (1986).

[13] R. Côté. *Ultra-Cold Collisions of Identical Atoms.* PhD dissertation, Massachusetts Institute of Technology, Department of Physics, February 1995. Full entry at http://dspace.mit.edu/handle/1721.1/32632.

[14] D. Griffiths. *Introduction to Quantum Mechanics.* Prentice Hall, (1995).

[15] R. Côté and A. Dalgarno. Phys. Rev. A **62**, 012709, (2000).

[16] A. Dalgarno. Philos. Trans. R. Soc. London, Ser. A **250**, 426, (1958).

[17] G. B. Arfken and H. J. Weber. *Mathematical Methods for Physicists.* IAP Harcourt Academic Press, (2001).

[18] J. L. Basdevant and J. Dalibard. *The Quantum Mechanics Solver.* Springer-Verlag, (2006).

[19] R. Maruyama, R. H. Wynar, M. V. Romalis, A. Andalkar, M. D. Swallows, C. E. Pearson, and E. N. Fortson. Phys. Rev. A **68**, 011403, (2003).

[20] B. J. Shields. *Loading a Planar RF Paul Trap From a Cold Yb$^+$ Source.* Bachelor thesis, Massachusetts Institute of Technology, Department of Physics, May 2006.

[21] D. Budker, D. K. Kimball, and D. P. DeMille. *Atomic Physics.* Oxford, (2004).

[22] D. J. Berkeland, J. D. Miller, J. C. Bergquist, W. M. Itano, and D. J. Wineland. J. Appl. Phys. A **83**, 10, (1998).

[23] G. R. Janik, J. D. Prestage, and L. Maleki. J. Appl. Phys. A **67**, 10, (1990).

[24] M. Drewsen, I. Jensen, J. Lindballe, N. Nissen, R. Martinussen, A. Mortensen, P. Staanum, and D. Voigt. Int. J. of Mass. Spec. **229**, 83-91, (2003).

[25] K. L. Corwin, Z. T. Lu, C. F. Hand, R. J. Epstein, and C. E. Wieman. App. Opt. **37**, 3295, (1998).

[26] S. Gasiorowicz. *Quantum Physics.* John Wiley & Sons, (2003).

[27] J. J. Sakurai. *Modern Quantum Mechanics.* Addison-Wesley, (1994).

[28] E. W. McDaniel. *Collision Phenomena in Ionized Gases.* John Wiley & Son, (1964).

[29] J. D. Jackson. *Classical Electrodynamics.* John Wiley & Son, (1998).

[30] H.S.W. Massey and R.A. Smith. Proc. R. Soc. London, Ser. A, Containing Math. and Phys. Char. **142**, 846, pp. 142-172, (1933).

[31] R. H. Barnett, S. Cox, and Larry O'Cull. *Embedded C Programming and the Atmel AVR.* CENGAGE Delmar Learning, (2006).